BMC Cardiovascular Disorders

RESEARCH

Open Access

Integrated bioinformatic and in vivo analysis confirms the cardioprotective role of OPA1

Claire Fong-McMaster[1,2,3], Serena M. Pulente[1,3], Luke S. Kennedy[1,2], Tyler K.T. Smith[1,2,4], Stephanie Myers[1,2], Michel N. Kanaan[1,2], Charbel Y. Karam[1,2], Matthew Cope[1,2,5], Michelle M. Levesque[1,2,3], Ella McIlroy[1,2], Ilka Lorenzen-Schmidt[3], Craig J. Goergen[6], Morgan D. Fullerton[1,2,4], Miroslava Cuperlovic-Culf[1,2,7], Erin E. Mulvihill[1,2,3*] and Mary-Ellen Harper[1,2*]

Abstract

Background OPA1 is an inner mitochondrial membrane protein that mediates diverse signaling processes. OPA1 is important for cardiac function and protects against cardiac insults such as ischemia/reperfusion injury. We sought to further assess OPA1 in cardiac pathologies, hypothesizing that OPA1 will function in a protective manner in chronic heart failure.

Methods Integrated analyses of publicly available histological and transcriptomic data were used to identify functional associations between OPA1 and other genes of interest. To experimentally assess these associations, mice with a 1.5-fold whole body OPA1 overexpression (OPA1-OE) were subjected to a modified transverse aortic constriction surgery and underwent 2-dimensional and 4-dimensional echocardiography along with molecular analyses including high-resolution respirometry, enzymatic activities, flow cytometry and transcript level analyses.

Results Bioinformatic analyses of histological and transcript data from the GTEx database indicated that OPA1 expression levels vary in the human heart, where elevated OPA1 transcript levels were associated with fatty acid, branch chain amino acid and cardiac contractile gene signatures. These functional associations were further supported by in vivo findings showing that OPA1-OE mice displayed improved 2D ejection fraction, end systolic volume, end diastolic volume and 4D cardiac functional parameters including global peak circumferential and surface area strain compared to WT mice. As well, OPA1-OE mice displayed sustained transcript levels of fatty acid, branch chain amino acid and contractile markers and no induction of fibrotic transcript markers.

Conclusion These results further demonstrate the important role of OPA1 in supporting optimal cardiac function and highlight potentially protective contractile and metabolic signaling pathways.

Keywords Mitochondria, Optic atrophy protein-1, Mitochondrial fusion, Heart failure, 4-dimensional echocardiography

*Correspondence:
Erin E. Mulvihill
emulvihi@uottawa.ca
Mary-Ellen Harper
mharper@uottawa.ca
[1]Department of Biochemistry, Microbiology and Immunology, University of Ottawa, Ottawa, ON, Canada
[2]Ottawa Institute of Systems Biology, Ottawa, ON, Canada
[3]University of Ottawa Heart Institute, Ottawa, ON, Canada
[4]Centre for Infection, Immunity and Inflammation, University of Ottawa, Ottawa, ON, Canada
[5]Department of Medicine, Queen's University, Kingston, ON, Canada
[6]Weldon School of Biomedical Engineering, Purdue University, West Lafayette, IN, USA
[7]Digital Technologies Research Centre, National Research Council Canada, Ottawa, ON, Canada

Background

Heart failure affects over 50 million people worldwide with increasing rates attributable to complex etiologies and risk factors [1, 2]. Many pharmacological approaches exist for disease management which include the use of ACE inhibitors, beta blockers, diuretics and SGLT2 inhibitors [3]. These therapies, combined with non-pharmacological approaches such as diet and exercise, require complex individualized management that is further complicated by comorbidities. Given this landscape, characterizing the underlying mechanisms that contribute to reduced cardiac function at each disease stage is critical to enable the design of new and complementary therapeutic approaches. Emerging evidence points to the potential role of mitochondrial-targeted therapeutics to treat heart failure [4, 5]. Changes in mitochondrial metabolism are evident throughout the progression of heart failure and largely include dysfunctional substrate metabolism including impaired mitochondrial energetics, reactive oxygen species overload, and an imbalance in mitochondrial dynamics [6].

Mitochondria make up 30% of cardiomyocyte volume and undergo cycles of fusion and fission in response to altered energy status or cellular stressors [7]. This dynamic process involves inner mitochondrial membrane (IMM) and outer mitochondrial membrane (OMM) proteins, as well as proteins that tether to adaptor proteins on the OMM [8]. Fission is largely driven by this latter class of proteins, in which dynamin-related protein 1 (DRP1) is recruited to the OMM and constricts mitochondria, leading to mitochondrial fission. Fusion is driven by three GTPases, mitofusin 1 and 2 on the OMM, and optic atrophy protein-1 (OPA1) on the IMM. In addition to mediating mitochondrial fusion, OPA1 is linked to oxidative phosphorylation efficiency, cristae morphology, apoptotic signaling and calcium signaling [9, 10].

OPA1 undergoes alternative splicing, generating eight isoforms in humans. After import into mitochondria, OPA1 long forms (L-OPA1), which are membrane-anchored, can be further cleaved into short forms (S-OPA1) by two mitochondrial inner membrane proteases, YME1L and OMA1 [11]. L-OPA1 isoforms are required for mitochondrial fusion, while S-OPA1 isoforms can maintain cristae structure, energetics and mitochondria DNA independent of L-OPA1 [12, 13]. Both L-OPA1 and S-OPA1 are required for mitochondrial network morphology, involving a tight balance of fusion and fission. OPA1-dependent functions such as the maintenance of cristae architecture are also essential for mediating mitochondrial membrane potential, minimizing cytochrome c release, and mitigating sensitivity to mitochondrial permeability transition pore opening [14–16].

In both human and pre-clinical models of heart failure, OPA1 protein abundance in the heart is lower relative to healthy controls [17, 18]. OPA1 heterozygous mice exhibit impairments in contraction, cardiac output and contractile response when aged or subjected to pressure-overload [19, 20]. Underlying these functional changes are differential calcium handling within cardiomyocytes, abnormal mitochondrial ultrastructure, and altered electron transport chain activity. Conversely, increased OPA1 protein levels have been shown to be protective during acute myocardial injury by maintaining cristae structure and minimizing apoptotic signaling [15]. In addition, OPA1 processing by the proteases YME1L and OMA1 impacts cardiac function [21–23]. Mitochondrial substrate utilization is closely linked to mitochondrial dynamics, with evidence highlighting the role of fatty acids in increasing YME1L expression, limiting L-OPA1 cleavage and inhibiting mitochondrial fragmentation [24]. Cysteine residues of OPA1 are also sensitive to redox modifications in the myocardium which can contribute to mitochondrial dysfunction [25]. Despite knowing that decreased OPA1 worsens cardiac function, it is unclear how a subtle increase in expression, one that could be therapeutically achievable, would influence cardiac function in a chronic heart failure state.

Given the evidence implicating OPA1-mediated mechanisms in various heart failure models, we sought to further assess the links between OPA1 and cardiac pathologies. Using human and mouse in vivo data, we confirm and extend the roles of OPA1 in supporting cardiac function with links to metabolic and contractile pathways.

Methods

GTEx bioinformatic analyses

All bioinformatic analyses were carried out using Python (Version 3.8.18) with figures and plots generated via the matplotlib [26] and seaborn [27] libraries. All statistical tests were performed through their respective Scipy method [28]. All data and code for these analyses are available in our Github repository: https://github.com/lkenn012/OPA1_heart_GTEx.

GTEx gene expression analysis

Human left ventricle (LV) Genotype-Tissue Expression (GTEx) RNA-seq data were collected (TPM, v8) via the GTEx Portal API to identify samples within top and bottom quintiles of OPA1 expression. Samples without expression data for OPA1 were first removed, and then TPM values were normalized by trimmed mean of M-values (TMM) [29] using the conorm library (https://pypi.org/project/conorm/). Samples were selected irrespective of age with an equal number of males and females selected. Initially, all RNA-seq samples were

considered (n = 433), though after selecting top and bottom quintiles by OPA1 expression it was observed that top quintile data consisted exclusively of individuals classified as "Ventilator cases" within the Hardy scale cause of death categorizations [30]. Although "Ventilator cases" represents roughly half of all GTEx individuals, to avoid possible confounding factors in the analysis quintiles were again selected from just this subset of samples (n = 246). From this subgroup of GTEx samples, top and bottom quintiles were selected by OPA1 expression (n = 48 per group).

Histology images pathology

LV histology images for individuals in bottom and top OPA1 quintiles were obtained from the National Cancer Institute's Biospecimen Research Database [31]. Histology data were downloaded directly from the GTEx histology viewer (https://gtexportal.org/home/histologyPage) for comparison of pathologies noted in OPA1 quintile s. Occurrences of pathology categories of interest in each group were compared by chi-squared tests.

Differential gene expression analysis

Differentially expressed genes between OPA1 quintile groups were determined as those genes with TMM-normalized expression values with absolute median $\log_2$ fold change values greater than 1.5 and false discovery rates < 0.01 as computed by Wilcoxon's rank sum test after adjusting for multiple testing by Benjamini-Hochberg correction (Statsmodels [32]). Genes with unusually large $\log_2$ fold changes (>8 or <−8) were also excluded as these come from comparisons to samples with no expression of the gene.

Supervised machine learning feature selection

Relevant genes associated with OPA1 expression were determined by PLS-DA [33] for classifying top and bottom quintile GTEx expressors, or as predictors of OPA1 expression across top and bottom quintiles by the multi-round Relief-based approach, TuRF [34, 35]. The PLS-DA algorithm was implemented using the scikit-learn [36] "PLSRegression" function, with default parameters using z-score normalized gene expression values as features and quintile groups as targets. The multi-round TuRF regression algorithm [35] was implemented via skrebate [37] with default parameters (using all samples as neighbours for computing weights) and the ReliefF algorithm [38] as a base (single-round) estimator to predict OPA1 expression across top and bottom expressors.

Relevant features were selected according to peak model performance over VIP score thresholds [39] for PLS-DA (2.00) and according to a selected relevance threshold >0 (0.100) for Relief features [40].

Gene-set enrichment analysis

Enriched functional terms in important genes for *OPA1* expression, defined as the overlapping gene set identified by differential expression and feature selection methods, were identified by ShinyGO [41] (version 0.80). All genes expressed in GTEx LV samples were used as background and an FDR cutoff of 0.01, and minimum pathway size of 10 were applied to gene ontology [42] term enrichment analysis to identify the top 20 enriched terms and corresponding values for each.

Interaction networks

The STRING database [43, 44] was used to construct knowledge and literature based interaction networks between the overlapping gene sets in our GTEx analysis. Networks were constructed based on a high confidence threshold defined by STRING using all interactions sources, with edge thickness proportional to the level of interaction evidence from the various sources.

Animal studies

All experiments involving mice were conducted in accordance with the principles of the Canadian Council of Animal Care and were approved by the Animal Care Committee of the University of Ottawa (UOHI-AUP-2909 and AUP-4381). OPA1-OE mice were a kind gift from Dr. Luca Scorrano [15, 45]. Male animals were housed in 12 h/12hr light cycle at 23 °C, with *ad libitum* access to standard chow (Harlan Teklad 2019) and water. Mice were euthanized by CO_2 inhalation.

OPA1-OE mice were genotyped using the following primers:

Transgenic allele (expected size 1200 bp):

M_OPA1TG_FWD: 5′-GCA ATG ACG TGG TCC TGT TTTG-3′

M_OPA1TG_REV: 5′-GAT AGG TCA GGT AAG CAA GCA AC-3′

Wildtype allele (expected size 400 bp):

M_WT_FWD: 5′-CTC CGG AAA GCA GTG AGG TAA G-3′

M_WT_REV: 5′-GAG GGA GAA AAA TGC GGA GTG-3′

Transverse aortic constriction model

Pressure-overload was induced using a modified transverse aortic constriction model. Mice were prepared with three analgesics – buprenorphine (0.05 mg/kg S.C. 60 min prior to surgery; Meloxicam, 1 mg/kg, S.C. 60 min prior to surgery and daily for 3 consecutive days; Buprenorphine Slow Release (lasting 72 h), 1.2 mg/kg, S.C. prior to start of surgery). Isoflurane (2–4%) was used as the anesthetic throughout the surgical operation. Mice were intubated using a 20-gauge intravenous catheter attached to a ventilator set to 130–150 breaths/min

with a tidal volume of 0.2mL. Once a sterile incision site was prepared, a transverse incision was made and both layers of the thoracic muscles were separated. The chest cavity was opened at the level of the second intercostal space and a chest retractor was used to spread the opening. The descending aorta was bluntly dissected out visually and a 6 – 0 silk was passed around the aorta using a Surgipro needle. The silk was tightened around a blunted 26 g needle placed parallel to the aorta and secured with two knots. The chest retractor was removed, and the chest cavity was closed with a 6 – 0 suture tie. Mice remained on the ventilator until spontaneous breathing and received a 0.5 mL saline (37 °C) injection S.C. Mice were monitored in an incubator (30 °C) with supplemental oxygen (1–2 L/min) and then returned after recovery to the standard housing rooms.

2D and 4D echocardiography

Cardiac function was measured using a Vevo3100 System with an MX400 transducer (FUJIFILM VisualSonics, Toronto). Mice were anesthetized using 1.5 –3% isoflurane and 1.5 L/min oxygen. Heart rate, respiratory rate and body temperature were monitored throughout all 2D and 4D imaging. 2D images in PLAX B mode and SAX B and M mode were taken at baseline, 5 weeks, 8 weeks and 12 weeks post-TAC surgery. Vevo LAB (5.8.2) was used for all 2D analyses.

4D mode was used to acquire SAX 4D images using a step size of 0.127 mm and frame rate of 400 Hz. 4D strain parameters were analyzed as previous described [46–48] using a custom MATLAB (MathWorks, USA) graphical user interface.

Electrocardiogram analysis

Surface ECG signals were acquired during 2D echocardiography imaging from four limb electrodes. Physiological data including time (ms) and ECG (mV) were exported from Vevo LAB (5.8.2) and analyzed using LabChart 8.0 (AD Instruments). The ECG analysis module was used to identify ECG parameters from 4 averaged beats over 3–5 cycles. Manual correction from incorrectly annotated waveforms was done using the IMPC waveform annotation [49].

Histological analyses

Heart tissue was fixed in 10% formalin and processed for paraffin-embedding. 4 µm sections were stained with Masson's trichrome to assess collagen. ImageJ Software and the Color Deconvolution tool was used to quantify interstitial and perivascular fibrosis. For analyses of cardiomyocyte cross sectional area, 4 µm sections were stained with wheat germ agglutinin (ThermoFisher, W11261) and analyzed using Cellpose [50] and ImageJ.

High resolution respirometry in permeabilized cardiac fibers

Cardiac myofiber mitochondrial oxygen consumption was measured using the Oxygraph-2k with an attached fluorometer (OROBOROS Instruments, Innsbruck, Austria). Left ventricular apex tissue was isolated and immediately placed in a 60 mm dish containing BIOPS buffer (in mM: CaK_2EGTA 2.77; K_2EGTA 7.23; Na_2ATP 5.77; $MgCl_2{}^*6H_2O$ 6.56; taurine 20; Na^{2+}2-phosphocreatine 15; imidazole 20; DTT 0.5; MES 50; pH 7; 4 °C). Cardiac myofibers were gently teased apart using fine-tip forceps and transferred to a 24 well plate. Fibers were permeabilized using 50 µg/ml saponin in BIOPS for 30 min. Fibers were washed three times in Miro5 buffer (0.5 mM ethylene glycol tetraacetic acid, 3 mM $MgCl_26H_2O$, 20 mM taurine, 10 mM KH_2PO_4, 20 mM N-2-hydroxyethylpiperazine-N-2-ethane sulfonic acid, 110 mM d-sucrose, 0.1% bovine serum albumin and 60 mM lactobionic acid; pH 7.1, 4 °C) for 10 min. Fibers were blotted dry, weighed, and immediately added to the Oxygraph chambers. All samples were run in duplicate at 37 °C with a stirring speed of 750 rpm. Hydrogen peroxide emission was measured simultaneously using the fluorimeter with the LED2-Module (525 nM) following the addition of 10 µM Amplex UltraRed (Invitrogen, A36006), 1 U/mL horseradish peroxidase (HRP) and 5 U/mL superoxide dismutase (SOD). The following SUIT protocol was used to assess mitochondrial bioenergetic function: malate (2 mM), palmitoyl carnitine (5mM) (FAO Leak), ADP (5 mM), Mg^{2+} (5 mM) (FAO OXPHOS), pyruvate (5 mM), glutamate (10mM), ADP (5 mM), Mg^{2+} (5 mM) (FAO + CI OXPHOS), succinate (10 mM) (FAO + CI + CII OXPHOS), ADP (5 mM), Mg^{2+} (5 mM), Oligomycin (2 µg/mL) (FAO + CI + CII Leak). All values were corrected for non-mitochondrial respiration.

Enzyme activities

Citrate synthase activity was measured in protein lysates, as previously described [51]. Briefly, activity was measured by calculating the rate of absorbance at 412 nM in 50 mM Tris-HCl (pH 8.0), with 0.2 mM DTNB, 0.1 mM acetyl-CoA and 0.25 mM oxaloacetate as the starter chemical using the BioTek Synergy Mx Microplate Reader (BioTek Instruments Inc). Enzyme activity was calculated using the extinction coefficient of 13.6 $mM^{-1}cm^{-1}$ for citrate synthase.

Mitochondrial/nuclear DNA ratio

DNA was isolated from LV tissue as previously described [52]. Briefly, tissue was homogenized in DNA lysis buffer (5 mM EDTA, 0.2% SDS, 200 mM NaCl, 100 mM Tris, pH 8.0) and incubated overnight with proteinase K (ThermoFisher, #25530049). DNA was extracted using phenol/

chloroform/isoamyl alcohol (25:24:1; PCIAA) and concentrations were measured using the Nanodrop 2000 (ThermoFisher). qPCR was run using the SsoAdvanced Universal SYBR Green Supermix (Bio-Rad, #1725272) and run on the CFX96 (Bio-Rad) according to manufacturer's protocol. Mitochondrial-encoded gene (*Nd1* and *16sRNA*) Ct values were normalized to nuclear-encoded genes (*Hk2* and *B2m*) using the $^{\Delta\Delta}$Ct method [53]. Primer sequences are shown in Table S1.

RNA extraction and quantitative PCR

Flash frozen LV tissue was homogenized in Trizol (ThermoFisher, #15596026) using the MagNA Lyser (Roche, Germany). RNA was isolated according to manufacturer's instructions and equalized using Ultrapure H_20 (ThermoFisher, #10977015). cDNA was synthesized using the All-In-One 5X RT MasterMix (ABM, #G592). qPCR was performed using the SsoAdvanced Universal SYBR Green Supermix (Bio-Rad, #1725272) and run on the CFX96 (Bio-Rad). Relative transcript expression was calculated using the $^{\Delta\Delta}$Ct method [53]. Genes of interest were normalized to the geometric mean of the Ct values of *B2m* and *Eef1e1*. Primer sequences are shown in Table S1.

Protein extraction and western blotting

Flash frozen LV tissue was homogenized in 1X RIPA buffer (Millipore, 20–188) supplemented with protease and phosphatase inhibitor cocktail (ThermoFisher Scientific #78440). Protein concentration was measured using a BCA protein assay kit (ThermoFisher, #23225) according to manufacturer's instructions. Samples for immunoblotting were prepared with SDS-PAGE loading buffer (50mM Tris-Cl (pH 6.8), 100mM DTT, 1.5% SDS, 0.01% Bromophenol blue, and 8.33% glycerol) and boiled at 95 °C for 5 min. SDS-PAGE was used to separate proteins, and proteins were transferred to nitrocellulose membranes and blocked in 5% BSA at room temperature for 1 h. Membranes were incubated in primary antibodies (OPA1, 1:1000, BD Biosciences, #612607), α-tubulin (1:2000, Protein Tech, #11224-1AP)) overnight. Membranes were incubated with an HRP-conjugated ECL substrate (Millipore, #WBLUC0500). Images were acquired using the ChemiDoc™ MP Imaging System (Bio-Rad). Densitometry analysis was done using Image Lab 6.1 (Bio-Rad).

Bone marrow single cell suspension preparation and flow cytometry staining

The tibia and femur from both legs were removed and placed in ice cold 1% FBS/PBS. The ends of the bones were cut, and one femur and one tibia were placed into a 0.5 ml tube that was punctured with a 27-gauge needle and contained within a 1.5 ml mini tube. The bones were then centrifuged at 10,000 x g for 1 min into 100 µl 1% FBS/PBS. Pellets were resuspended in 1 ml of room temp RBC lysis buffer (155 mM NH_4Cl (MilliporeSigma #A9434), 10 mM $NaHCO_3$ (BioShop #SOB308), 10 mM EDTA) and incubated at room temperature for 2 min. The suspension was passed through a pre-wetted 100 µm filter followed by 10 ml of ice cold 1% FBS/PBS. The cells were centrifuged and resuspended in 2 ml of 1% FBS/PBS, before being counted using Trypan blue and a hemocytometer. Single cell suspensions from bone marrow were transferred to 1.2 ml cluster tubes (Corning #4401). Cells were centrifuged at 400 x g for 5 min and then stained with Zombie Aqua (1:500; BioLegend #423102) for live/dead discrimination in 50 µl PBS for 30 min on ice. No blocking was performed with CD16/32 because it was a marker in the progenitor stain. Cells were washed with PBS, centrifuged, and stained with primary antibodies diluted in PBAE (1% BSA, 2 mM EDTA, 0.05% sodium azide (Ricca #7144.8–16) in PBS) for 20 min on ice protected from light. Primary antibodies from BioLegend: Sca1-BV605 (1:200; #108134), CD16/32-BV711 (1:200; #101337), biotinylated lineage antibodies (CD3e, Gr-1, B220, TER-119, CD11b; all at 1:100; #133307), CD135-PE (1:200; #135306), CD150-PE-Dazzle (1:200; #115936), CD48-PE-Cy7 (1:200; #103424). Primary antibodies from Thermo Fisher: CD34-eF660 (1:100; #50–0341-82), cKit-APC-eF780 (1:200; #47–1171-82). Cells were washed with PBS and secondary antibody (streptavidin-AF488 (1:200; BioLegend #405235) for another 20 min on ice. Cells were washed in PBS, centrifuged, and fixed with 2% PFA/PBS for 15 min on ice. The cells were washed a final time with PBS, then resuspended in PBAE for analysis on a LSR Fortessa (BD Biosciences) flow cytometer.

Statistical analysis

For GTEx analyses, all statistical tests were computed through their respective Scipy method [28]. Comparison of overall GTEx gene expression was done by Mann-Whitney U test [54] and OPA1 expression in young and old samples by two-sample T-test [55]. Chi-square test was used to compare pathology occurrence in groups of GTEx histological data [56].

Unless stated or specified, all data are shown as mean ± SEM. GraphPad Prism software 10.2.3 was used for all statistical analyses of the in vivo results. For analyses comparing two groups, an unpaired two-tailed Student's t-test was used. In all experiments containing two factors (genotype and surgical intervention), data were analysed using a two-way ANOVA with Tukey's *post-hoc* tests.

Results

OPA1 transcript levels associate with contractile and metabolic pathways in human left ventricle tissue

To explore *OPA1* gene expression and associated mechanisms in the heart, we first assessed human gene expression profiles using the GTEx Portal [57, 58] (Fig. 1A). RNA sequencing data from GTEx male and female LV samples were filtered based on *OPA1* expression levels. Top and bottom quintiles of *OPA1* expression were defined from all samples (n = 246 samples, see methods for full description of sample inclusion criteria). Interestingly, a wide range of *OPA1* transcript expression was observed in the GTEx LV samples (Fig. 1B), with a median $\log_2$ fold change difference of 1.72 between top and bottom quintiles despite a minimal difference in overall gene expression profiles between the groups (Fig S1A). Given the role of mitochondrial metabolism and dynamics in cardiac aging [59, 60], we assessed any potential differences in *OPA1* transcript across all ages. In line with previous literature in human skeletal muscle [61], we observed a trend of decreased *OPA1* expression in LV samples aged 50–79 compared to LV samples isolated from those aged 20–49 (Fig S1B).

To explore underlying gene signatures in the LV samples from the top and bottom *OPA1* quintiles, we identified gene expression changes corresponding with *OPA1* levels. Three approaches including differential expression analysis, partial least squares discriminant analysis (PLS-DA) [33] and Relief-based analysis were used to identify statistically relevant genes [34, 35]. 441 and 488 genes were positively and negatively differentially expressed, respectively, according to the $\log_2$ fold change and associated p-values between the *OPA1* quintiles in LV (Fig. 1C). In other words, the expression of 441 genes was higher in the upper quintile of *OPA1* expression compared to the lower quintile and 488 genes had lower expression in the top quintile compared to the bottom *OPA1* quintile. Two machine learning methods (PLS-DA and TuRF algorithms) identified 3582 and 3427 important feature genes, respectively, using variable importance projection (VIP) scores [39] ≥ 2.00 for PLS-DA (Fig S1C) and relevance thresholds ≥ 0.10 for TuRF. Across these three computational methods, we identified 229 common genes that positively associate with *OPA1* expression. Conversely, we only detected 31 common negatively associated genes with *OPA1* expression.

To determine the functional relevance of these OPA1-dependent genes, gene ontology enrichment was applied to the positively associated and negatively associated gene sets using GO Biological Process and GO Cellular Component terms. Cardiac muscle contractile functions were enriched in the positively associated gene set (Fig. 2A).

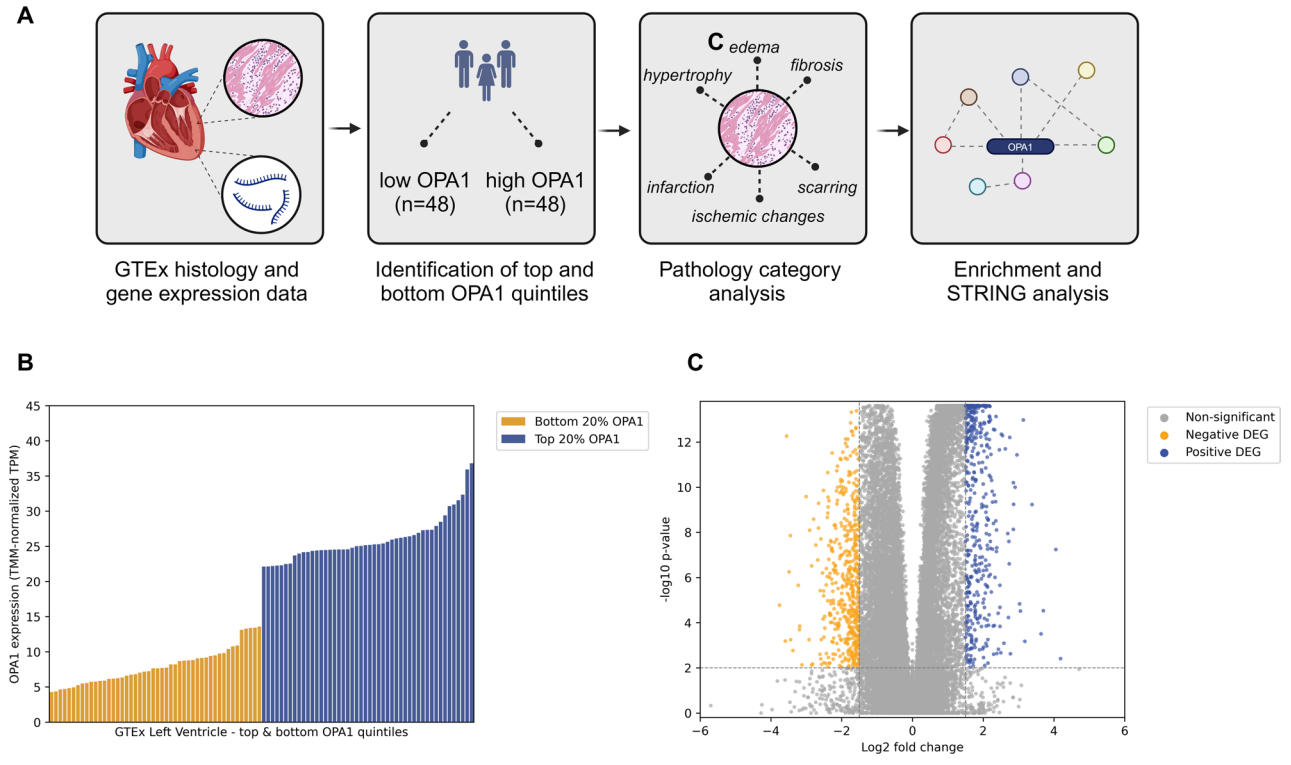

Fig. 1 OPA1 expression in top and bottom quintiles of GTEx human left ventricle samples. (**A**) Schematic of GTEx data processing and analysis. (**B**) Normalized expression values of OPA1. (**C**) Differential gene expression between top and bottom quintiles of OPA1 expression. Significance thresholds are 1.5 median log2 fold change and 0.01 adjusted p-values. n = 48 per quintile

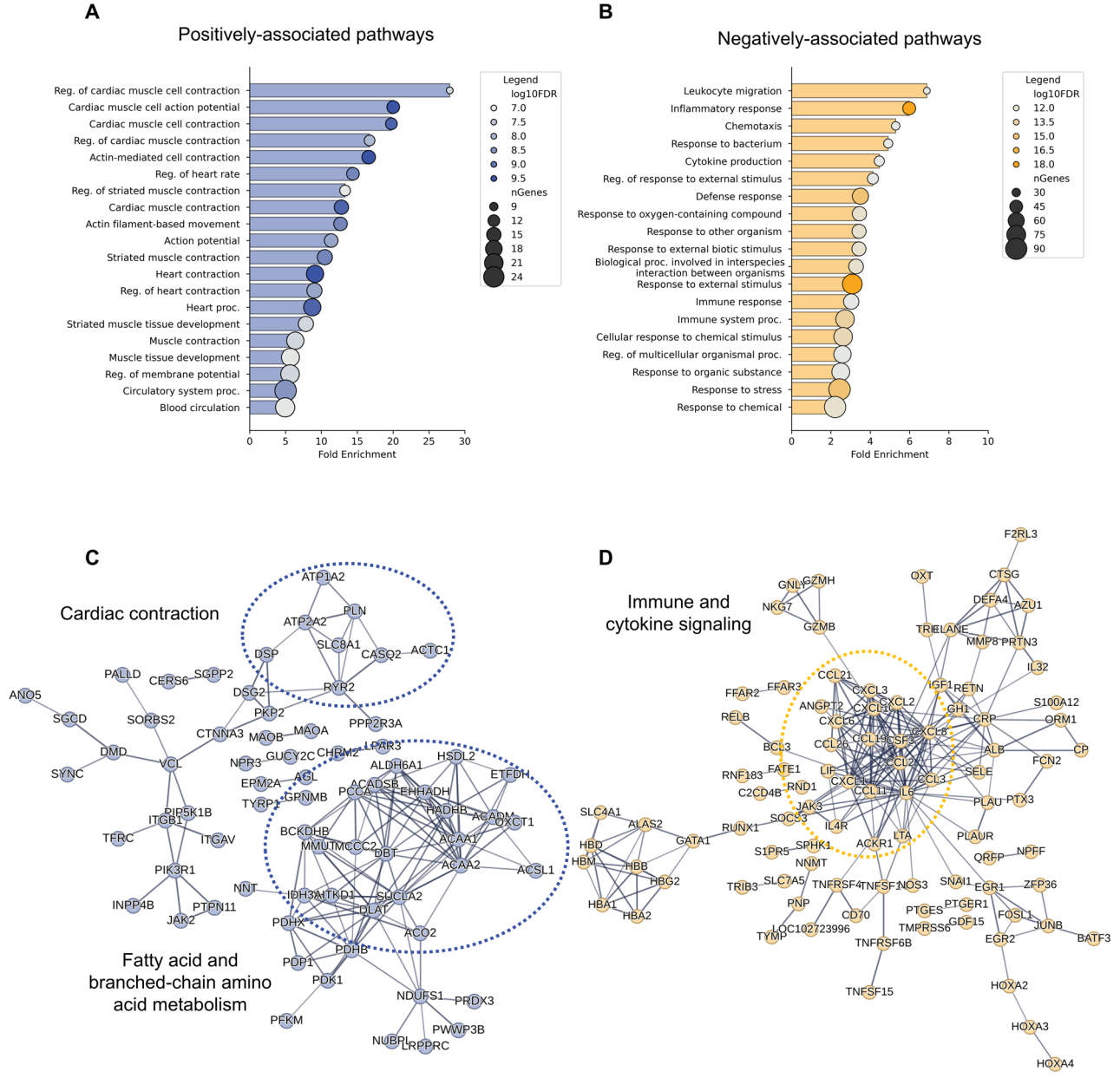

Fig. 2 Differential gene signatures between top and bottom OPA1 quintiles of GTEx human left ventricle samples. (**A-B**) Enriched GO biological process terms for genes with expression levels negatively and positively associated with OPA1 expression when comparing top and bottom OPA1 expressors. (**C-D**) Protein-protein interaction network of negative and positive DEGs. Edges are defined by interaction confidence through STRING evidence sources. $n = 48$ per quintile

For example, the GO terms regulation of cardiac muscle cell contraction and cardiac muscle cell action potential had the highest fold enrichment amongst the positively associated pathways. Genes that were identified in the positively enriched pathways included *ATP1A2*, *ATP2A2*, *RYR2*, *ACADM* and *BCKDHB* (Supplemental File 1). Due to the limited gene set size, enrichment analysis for the negatively associated genes was performed using the 488 statistically down-regulated genes identified by differential expression analysis. Interestingly, immune responses including leukocyte migration and inflammatory response most strongly negatively associated with *OPA1* expression (Fig. 2B). In these pathways, down-regulated genes from the differential expression analysis included *IL6*, *CXCL1*, and *CXCL2* (Supplemental File 1). In the most enriched cellular component GO terms, the sarcoplasmic reticulum, TCA complex, and contractile regions (Z disk, I band) were associated with *OPA1*, while hemoglobin was amongst the negatively associated genes (Fig S1D).

To expand the functional understanding of these gene enrichment signatures and how they relate to OPA1 expression, STRING [43, 44] interaction networks were used to identify relationships between differential genes through various associations, including protein-protein interaction, text mining, and homology. For the 229 genes that associated with high *OPA1* expression, distinct functional hubs are present in the protein-protein interaction networks with respect to fatty acid and branched chain amino acid metabolism (Fig. 2C), and immune and cytokine signaling terms for negatively associated genes (Fig. 2D).

OPA1 expression inversely correlates with cardiac pathology in human left ventricle tissue

To explore the relationship between *OPA1* transcript expression and cardiac pathologies, we returned to the GTEx portal, this time analyzing LV histological samples from top and bottom *OPA1* quintiles. Relevant pathology categories in the LV histology samples such as fibrosis, as identified by pathologists [62], were selected and their rates of occurrence were compared between the top and bottom *OPA1* expressors, as well as between all samples (Fig. 3A). Fibrosis was identified more frequently in the lowest *OPA1* expressing LV samples compared to higher expressing *OPA1* LV samples and compared to all LV samples (Fig. 3A).

OPA1 overexpression in mice preserves cardiac function following pressure overload-induced cardiac stress

Given the link between human *OPA1* expression and cardiac contractile and metabolic function-related genes, we followed up with in vivo work in a mouse model to assess how increased levels of OPA1 would impact cardiac function in response to a pressure overload-induced cardiac stress. To do so, we employed OPA1 overexpressing (OPA1-OE) mice, which exhibited a 1.5-fold whole body overexpression (protein level) [15], and subjected them to a modified transverse aortic constriction (TAC) surgery [63] (Fig. 4A-B). In this modified TAC model, banding is placed around the descending aorta using a 26-gauge needle, which produces a milder cardiac stress response than typical high TAC surgical models. Mice subjected to descending TAC surgery exhibited a heart failure phenotype at 12 weeks post-TAC when compared to sham-operated mice, with statistically significant increases in LV mass (Fig S2A), LV end diastolic diameter (LVEDD) (Fig S2B), and LV end systolic diameter (LVESD) (Fig

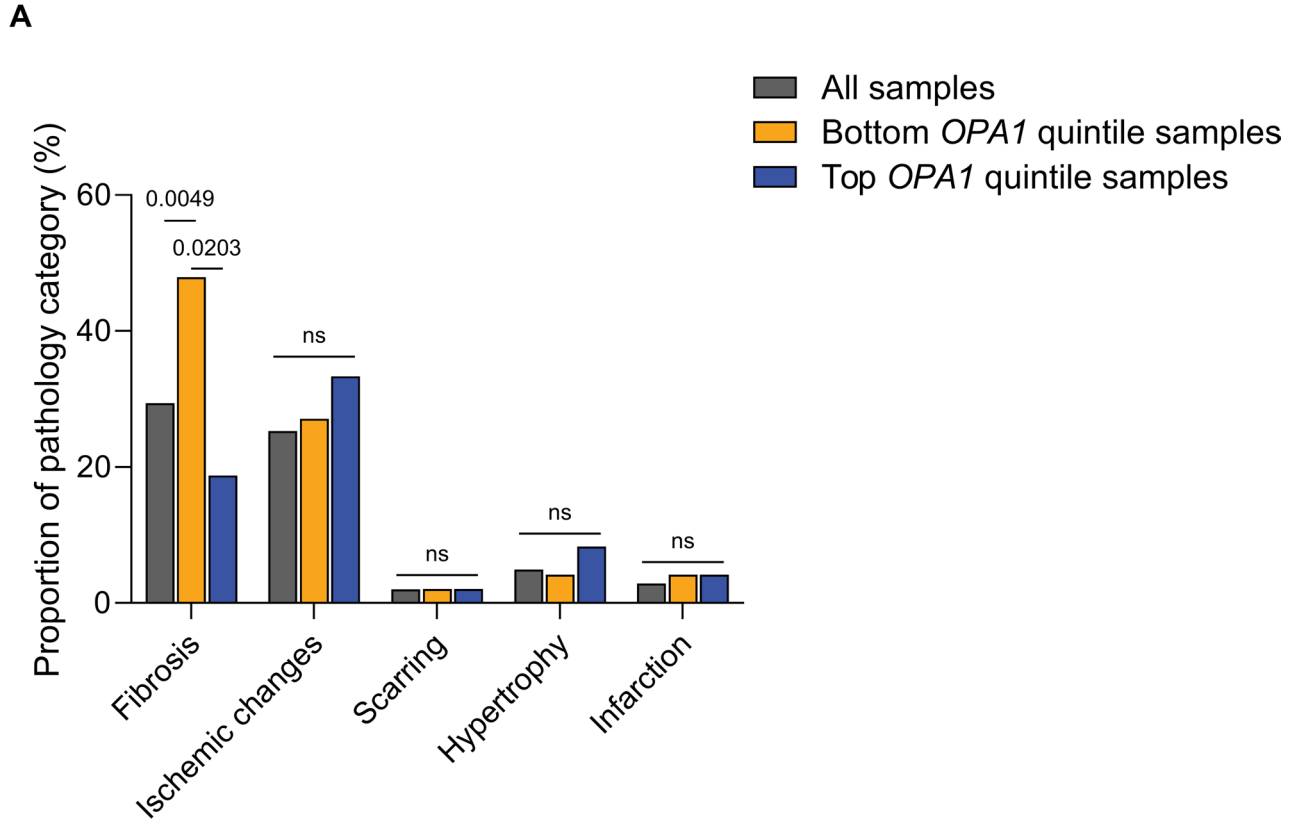

Fig. 3 Pathology assessment in top and bottom quintiles for OPA1 expression in GTEx human left ventricle samples. (**A**) Incidence of fibrosis, ischemic changes, scarring, hypertrophy, and infarction identified in pathology notes from H&E sections of human left ventricle samples from the top and bottom OPA1 expression quintiles. $n = 48$ per quintile

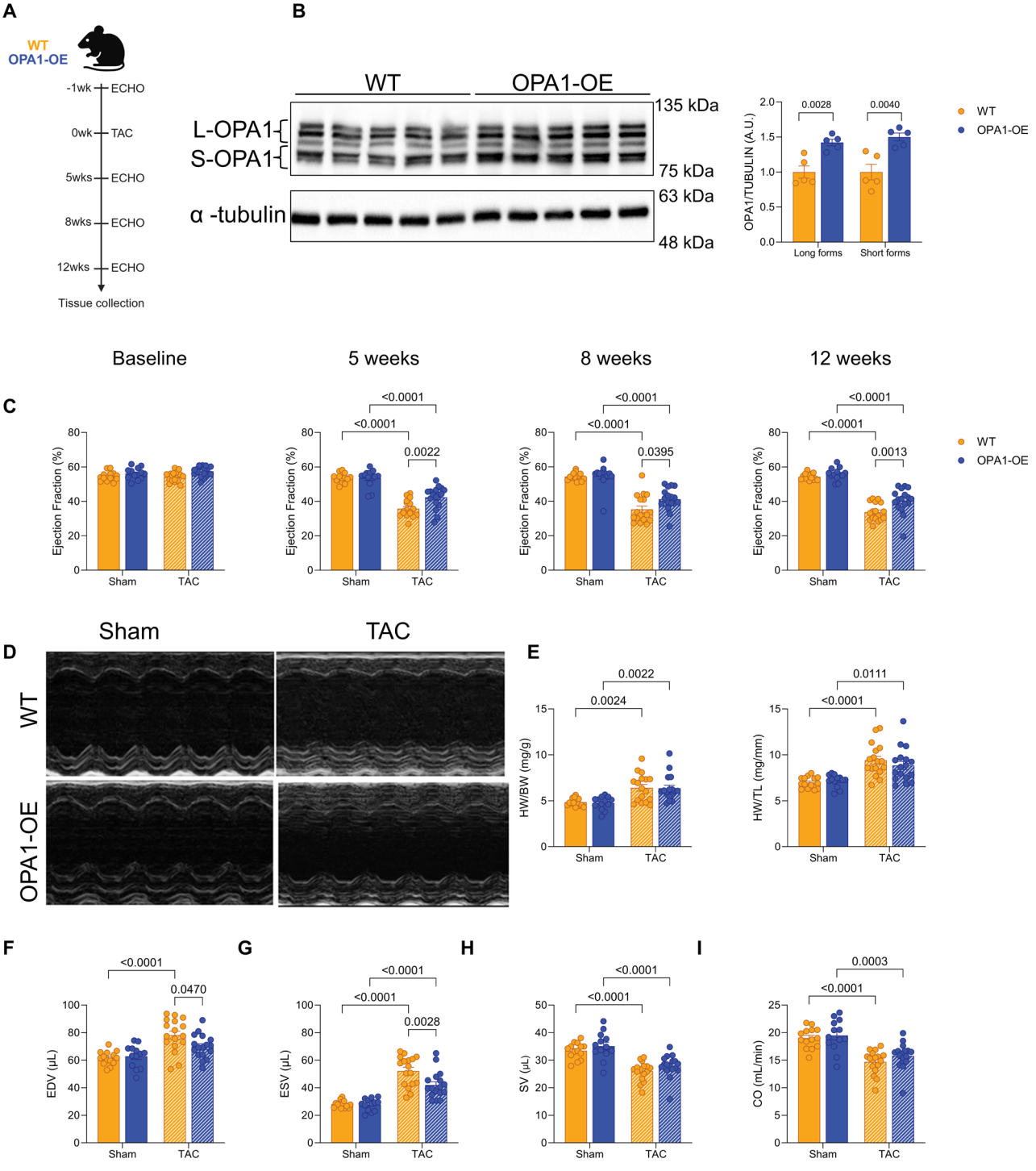

Fig. 4 OPA1 overexpression mediates cardiac functional protection in a murine model of pressure-overload. **A** Schematic of experimental design and study imaging timepoints. **B** Representative western blot of cardiac protein sample from wildtype (WT) and OPA1 overexpressing (OPA1-OE) mice and densitometry analysis. $n = 5$ per group. **C** Ejection fraction measured by 2D parasternal long axis at baseline, 5 weeks, 8 weeks, and 12 weeks post-TAC. **D** Representative short axis M-mode images. **E** Heart weight to tibia length ratio (HW/TL) and heart weight to body weight (HW/BW) ratio at 12 weeks post-TAC. **F-I** 2D parasternal long axis measurements including end diastolic volume (**F**), end systolic volume (**G**), stroke volume (**H**) and cardiac output (**I**) at 12 weeks post-TAC. $n = 13–17$ per group. All data are represented as mean ± SEM. P values calculated using an unpaired two-tailed Student's t-test for (B) and two-way ANOVA with Tukey's post-hoc analysis for (C, E-I). Full-length blots from (B) are presented in Supplementary Fig. 6

S2C), but no changes in lung weight (Fig S2D) or lung water content (Fig S2E). Electrocardiogram analyses at 12 weeks post-TAC confirmed the induction of cardiac remodeling as seen by elongation of the QRS interval (Fig S2F), QT interval (Fig S2G) and no changes in RR interval (Fig S2H) or PR interval (Fig S2I).

Mice of both genotypes were randomly assigned to receive descending TAC or sham surgery. At 5-, 8- and 12-weeks post-TAC, OPA1-OE mice had higher ejection fraction evaluated by parasternal long axis B-mode echocardiography compared to wildtype (WT) mice, indicative of improved cardiac remodeling (Fig. 4C). This was also supported by M-mode short axis imaging (Fig. 4D), which showed higher ejection fraction and cardiac output in OPA1-OE TAC mice compared to WT TAC mice (Fig S3A-B). Cardiac structural remodeling was evident in both WT and OPA1-OE TAC mice as both genotypes had significant increases in the heart weight/tibia length (HW/TL) and heart weight/body weight (HW/BW) ratios compared to sham mice (Fig. 4E). While both WT and OPA1-OE groups exhibited modest increases in end diastolic volume (EDV) with TAC, OPA1-OE EDV increased to a lesser extent than WT mice (Fig. 4F). The same trend held true for end systolic volume (ESV) (Fig. 4G). Conversely, there were no genotypic changes observed in stroke volume or cardiac output (Fig. 4H-I). These data suggest that increased OPA1 expression in mice is protective in maintaining cardiac function in response to a pressure overload-induced cardiac stress.

OPA1 overexpression maintains global cardiac functional parameters identified by 4D strain analysis in response to pressure overload-induced cardiac stress

While 2D imaging can be used to assess cardiac functional changes, volumetric measurements are estimated from only two planes of view. To fully characterize volumetric changes in response to TAC surgery, we employed 4D echocardiography, which collects a 3D image at every time point along the short axis using a step motor, allowing for analysis of myocardial kinetics and motion. Using a custom strain technique [46, 47] (Fig. 5A), we assessed global strain parameters at 12 weeks post-TAC in a subset of mice (Fig. 5B). Global circumferential strain magnitude decreased in both WT and OPA1-OE TAC mice compared to their respective sham mice, but to a lesser extent in OPA1-OE mice compared to WT TAC mice (Fig. 5C). There was decreased longitudinal strain magnitude in WT TAC mice compared to WT sham mice and no significant changes between other groups (Fig. 5D). Surface area strain magnitude was decreased in both WT and OPA1-OE TAC mice, but OPA1-OE TAC mice maintained surface area strain compared to WT mice (Fig. 5E). Finally, transmural (or radial) strain was decreased in both TAC genotypes compared to their respective sham mice, with no genotypic differences (Fig. 5F).

Minimal hypertrophic and fibrotic remodeling induced by descending TAC

Since we observed decreased fibrosis in our GTEx dataset in high *OPA1* expressors, we assessed markers of fibrotic and hypertrophic remodeling at 12 weeks post-TAC. However, we observed no changes in perivascular and interstitial fibrosis in response to the pressure overload induced by descending aortic banding in either genotype (Fig. 6A-C). In line with this minimal fibrotic phenotype, we observed no differences in cardiomyocyte cross-sectional area (CSA) between sham and TAC mice (Fig. 6A-D), although there were mild trends for increased levels of hypertrophy markers including *Nppb* in WT TAC mice compared to WT sham mice (Fig. 6E). Similarly, TAC induced modest increases in fibrosis markers including *Tgfb1*, *Col1a2*, and *Ctgf* in WT mice compared to sham mice (Fig. 6F). However, this was less apparent in OPA1-OE mice.

Contractile and metabolic transcriptional changes between OPA1-OE and WT descending TAC mice

Given that *OPA1* transcript levels were associated with contractile signaling markers in the GTEx human heart data, we assessed contractile markers in our in vivo study. *Atp2a2* transcript levels were significantly higher in OPA1-OE TAC mice compared to WT TAC mice (Fig. 7A). Another functional cluster identified from the genes associated with *OPA1* expression was fatty acid and branched chain amino acid (BCAA) metabolism. As metabolic remodeling in heart failure is complex and involves changes in substrate uptake, utilization and oxidative metabolism [64], we assessed transcript levels of fatty acid oxidation and BCAA markers. Markers of fatty acid metabolism including *Cd36* and *Acadm* were modestly decreased in WT TAC mice compared to WT sham mice, and *Cd36* was significantly lower in WT TAC compared to OPA1-OE TAC mice (Fig. 7B). BCAA markers including *Bcat2* and *Bckda* were lower in WT TAC mice, but *Bcat2* remained elevated in OPA1-OE TAC mice (Fig. 7C).

To investigate the functional implications of OPA1 overexpression to mediate metabolic changes in our mild heart failure model, we measured maximal oxygen consumption in permeabilized LV myofibers in response to saturating concentrations of palmitoyl carnitine/malate, glutamate/pyruvate, and succinate. Surprisingly, there were no changes between TAC and sham mice of either genotype (Fig S4A-E). Simultaneous measurement of hydrogen peroxide emission to assess reactive oxygen species, indicated no changes between TAC or sham mice of either genotype (Fig S4F-J). In addition,

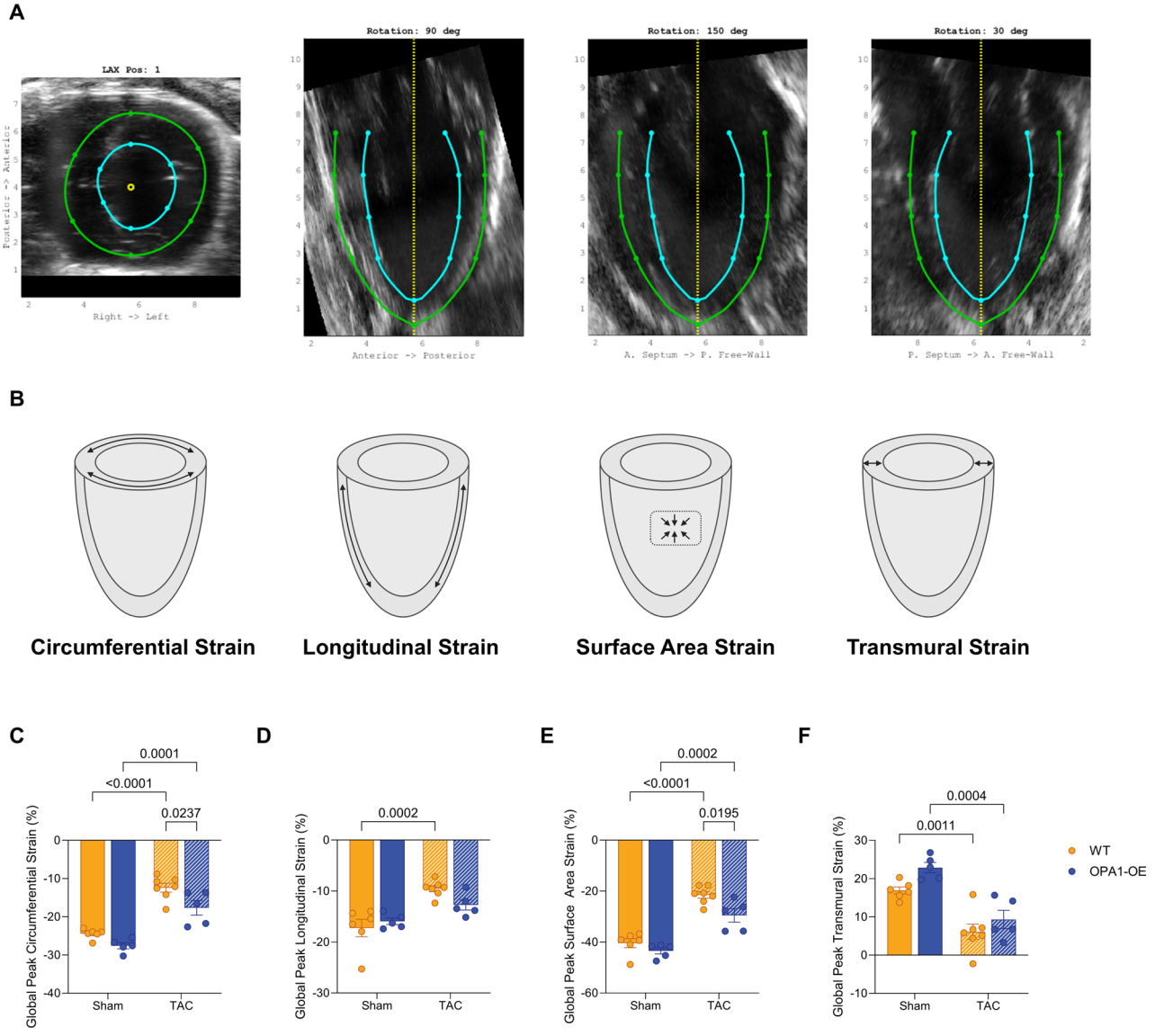

Fig. 5 4D strain analysis identifies changes in global strain parameters post-TAC in WT and OPA1-OE mice. **A** Representative 4D graphical user interface. **B** Schematic of global strain orientations. **C-F** Global strain parameters including circumferential (**C**), longitudinal (**D**), surface area (**E**), and transmural (**F**) at 12 weeks post-TAC. $n = 5–7$ per group. All data are represented as mean ± SEM. P values calculated using a two-way ANOVA with Tukey's post-hoc analysis for (**C**-**F**)

we measured mitochondrial DNA/nuclear DNA ratios and citrate synthase activity as indicators of mitochondrial content and observed no differences (Fig S4K-M), highlighting how the severe mitochondrial dysfunction typically observed in high TAC models [65–67] was not apparent in our descending TAC model.

Bone marrow hematopoiesis is minimally affected by descending TAC model

Immune cell-derived inflammation plays crucial roles in heart failure progression [68–70], though this is typically most evident in the myocardium within an acute period following TAC [71]. Because immune pathways were negatively associated with *OPA1* transcript expression, we wondered if OPA1 overexpression induced any longer-term effects on the immune system. Bone marrow hematopoiesis dynamically responds to environmental cues to continuously repopulate the circulating immune cell pool. To determine whether TAC or the overexpression of OPA1 induced long term inflammatory bias in bone marrow progenitor populations, we performed flow cytometry on hematopoietic populations in bone marrow at 12 weeks post-TAC (Fig S5A).

The hematopoietic stem and progenitor cells in the bone marrow can be divided into two main groups depending on their expression of cKit and Sca1: LSK

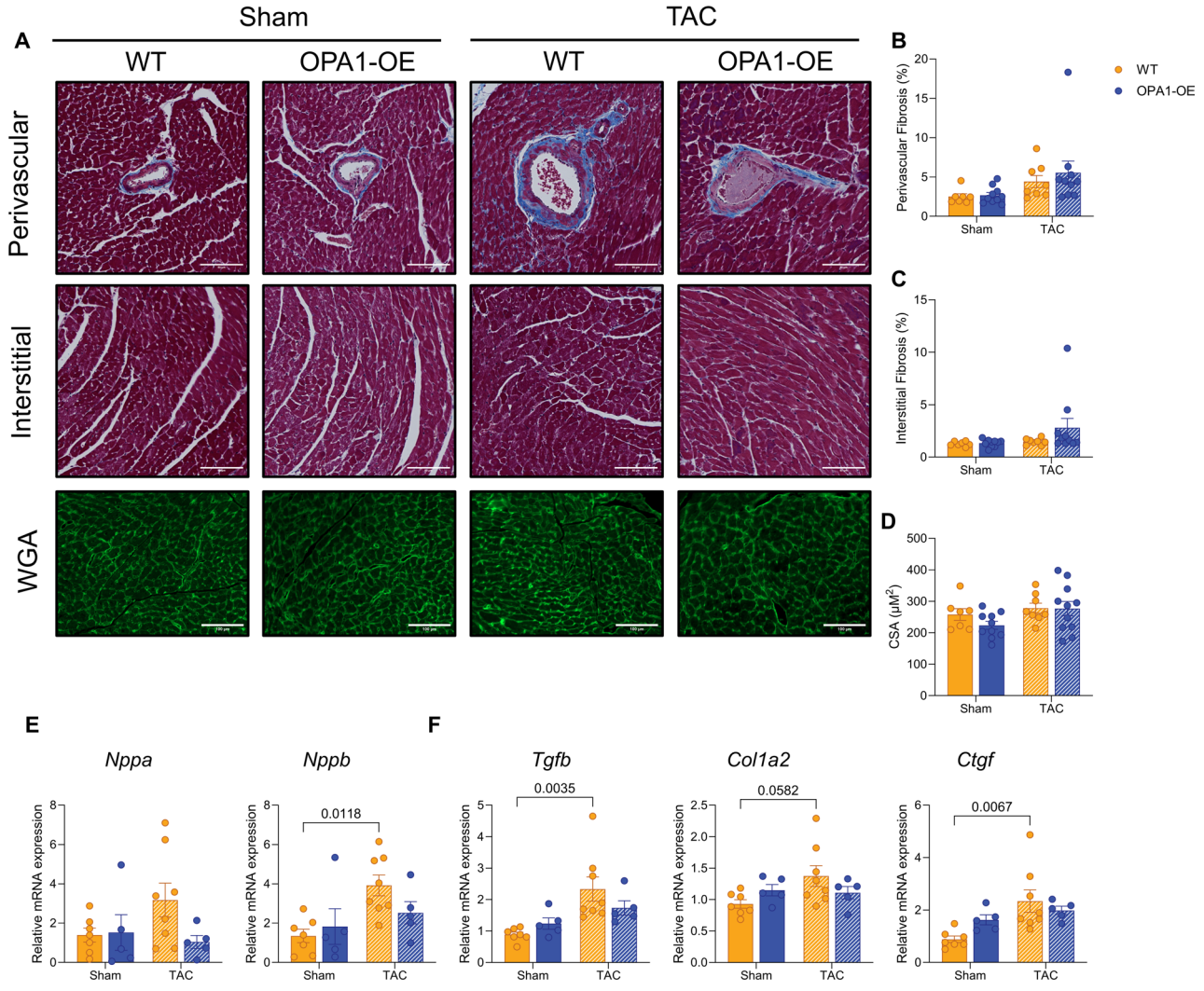

Fig. 6 Hypertrophic and fibrotic genes are upregulated in WT but not OPA1-OE TAC mice. **A** Representative images of Masson's trichrome and wheat germ agglutinin staining of LV cross sections. **B-C** Quantification of perivascular (**B**) and interstitial fibrosis (**C**) from trichrome-stained slides. **D** Quantification of cardiomyocyte cross-sectional area from wheat germ agglutinin stain. $n = 7–11$ per group. **E-F** Relative mRNA expression of hypertrophy markers (*Nppa* and *Nppb*) and fibrosis markers (*Tgfb*, *Col1a2*, and *Ctgf*) in cardiac tissue at 12 weeks post-TAC. All transcript data are expressed relative to the geometric mean of *B2m* and *Eef1e1*.$n = 5–8$ per group. All data are represented as mean ± SEM. P values calculated using a two-way ANOVA with Tukey's post-hoc analysis for (**B**-**F**)

cells, which express both cKit and Sca1 and are the most restricted group, and LK cells, which only express cKit and are more committed to the myeloid and erythroid lineages. The frequency of LK cells was mostly unchanged between both sham and TAC conditions and by genotype (Fig. 8A-D). However, there were slightly less CMP cells following TAC (Fig. 8C), and this corresponded with a slight relative increase in GMPs when examined as the frequency of LK cells (Fig. 8E). LSK cells, which include short- and long-term hematopoietic stem cells, as well as multipotent progenitors (MPP) that display myeloid bias (MPP3), lymphoid bias (MPP4), and erythroid bias (MPP2), largely did not differ in population frequency between surgery or genotype conditions (Fig. 8F-K). Although all three MPP populations trended lower with TAC regardless of genotype, this effect was driven by two sham mice that had elevated total LSK cells (Fig. 8L). Collectively, these data suggest that both pressure overload induced by descending TAC, and the mild overexpression of OPA1, have little effect on bone marrow hematopoiesis at an extended interval of chronic heart failure.

Discussion

The mitochondrial inner membrane protein OPA1 plays a critical role in maintaining cardiac function through multiple well-characterized pathways including modulating mitochondrial dynamics, preventing apoptosis, and promoting energy metabolism. Here, we provide evidence linking low *OPA1* transcript levels to advanced

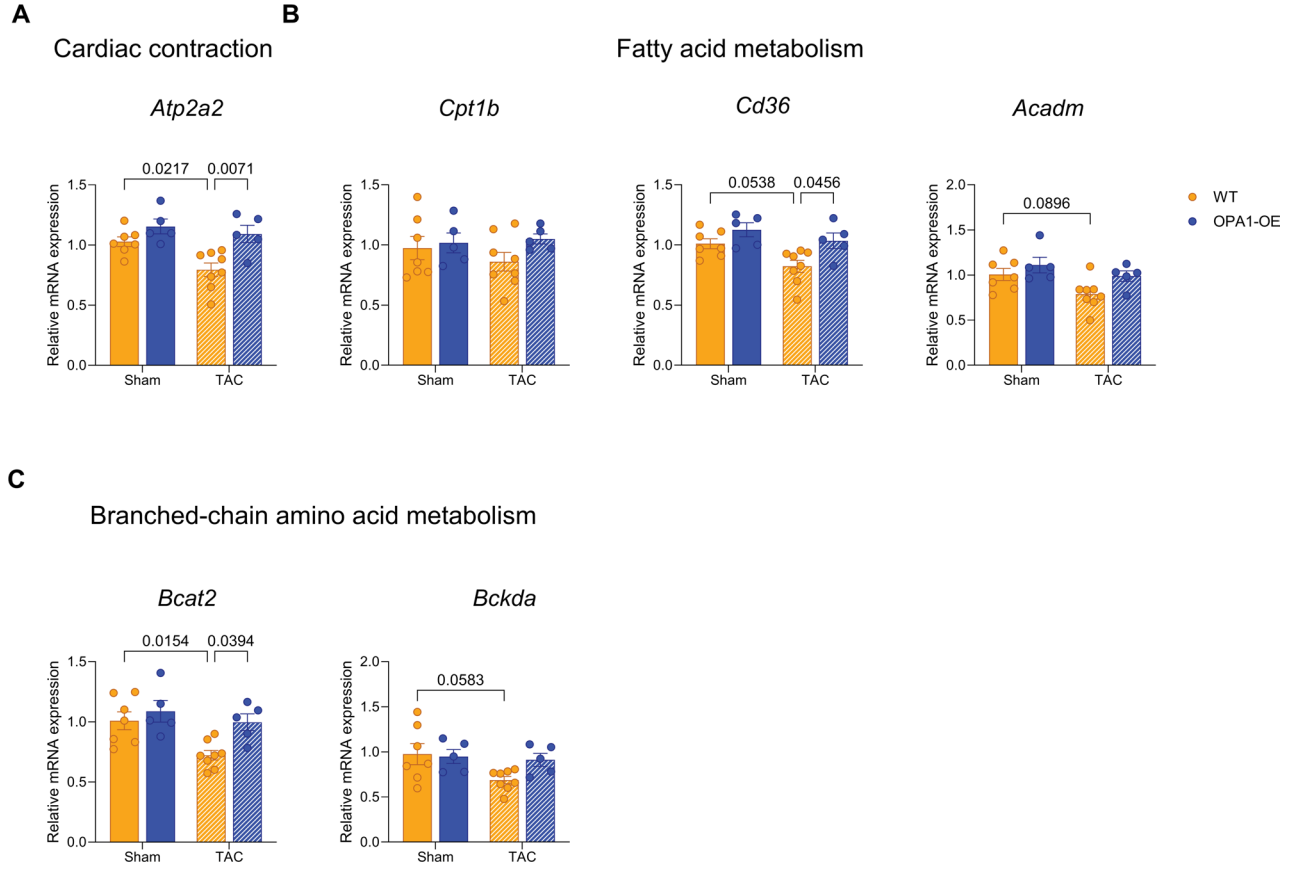

Fig. 7 Expression of contractile and metabolic-related genes are higher in OPA1-OE TAC mice. **A-C** Relative mRNA expression of contraction (*Atp2a2*) (**A**), fatty acid metabolism (*Cpt1b*, *Cd36*, and *Acadm*) (**B**), and branch chain amino acid metabolism (*Bcat2* and *Bckda*) (**C**) in cardiac tissue at 12 weeks post-TAC. All transcript data are expressed relative to the geometric mean of *B2m* and *Eef1e1*.*n* = 5–8 per group. All data are represented as mean ± SEM. P values calculated using a two-way ANOVA with Tukey's post-hoc analysis for (A-C)

characteristics of cardiac pathology in humans, specifically cardiac fibrosis. In addition, our analyses of publicly available transcriptomics data identified varied *OPA1* gene expression in the human heart and differentially expressed gene signatures amongst high and low *OPA1* expressing human LV tissue. Cardiac contractile functions were associated with high *OPA1* expression while immune signaling was associated with low *OPA1* expression. We further investigated these observations using a mouse model of modest OPA1 overexpression, where we observed less cardiac dysfunction in response to a descending aortic banding surgery along with sustained transcript levels of contractile and metabolic genes.

Previous work has highlighted the role for OPA1 in human heart failure pathology, identifying lower OPA1 protein levels in ischemic cardiomyopathy [17]. Our work linking low *OPA1* transcript levels with increased fibrosis in human LV samples further implicates the protective role of OPA1 signaling in heart failure progression. Cardiac pathologies can present in patients with autosomal dominant optic atrophy, a disease where up to 70–90% patients present with a mutation in OPA1 [72, 73]. These clinical reports have noted early-onset myocardial infarction [74], arrhythmia [75, 76], and hypertrophic cardiomyopathy [75], calling for the recommendation for further investigation into the connection between OPA1 mutations and cardiac events [75].

While the link between cardiac function and OPA1 has been assessed using heterozygous models [19, 20, 77], an OPA1 overexpression model [15], and models modulating upstream proteases or cleavage sites [21–23], our work is the first to increase OPA1 levels during a chronic in vivo heart failure model. Mild OPA1 overexpression maintained cardiac functional parameters including ejection fraction and fractional shortening, as well as circumferential and surface area strain post-TAC compared to WT mice (Figs. 4 and 5). These results align with data showing that OPA1 heterozygous mice are more sensitive to pressure overload and ischemia/reperfusion [19, 77]. Original characterization of the OPA1-OE mouse model [15] identified no baseline changes in cardiac function or structure at 5 months and protection from ischemia [15]. When aged to 9 months, these mice develop non-pathological hypertrophy as indicated by an increased HW/

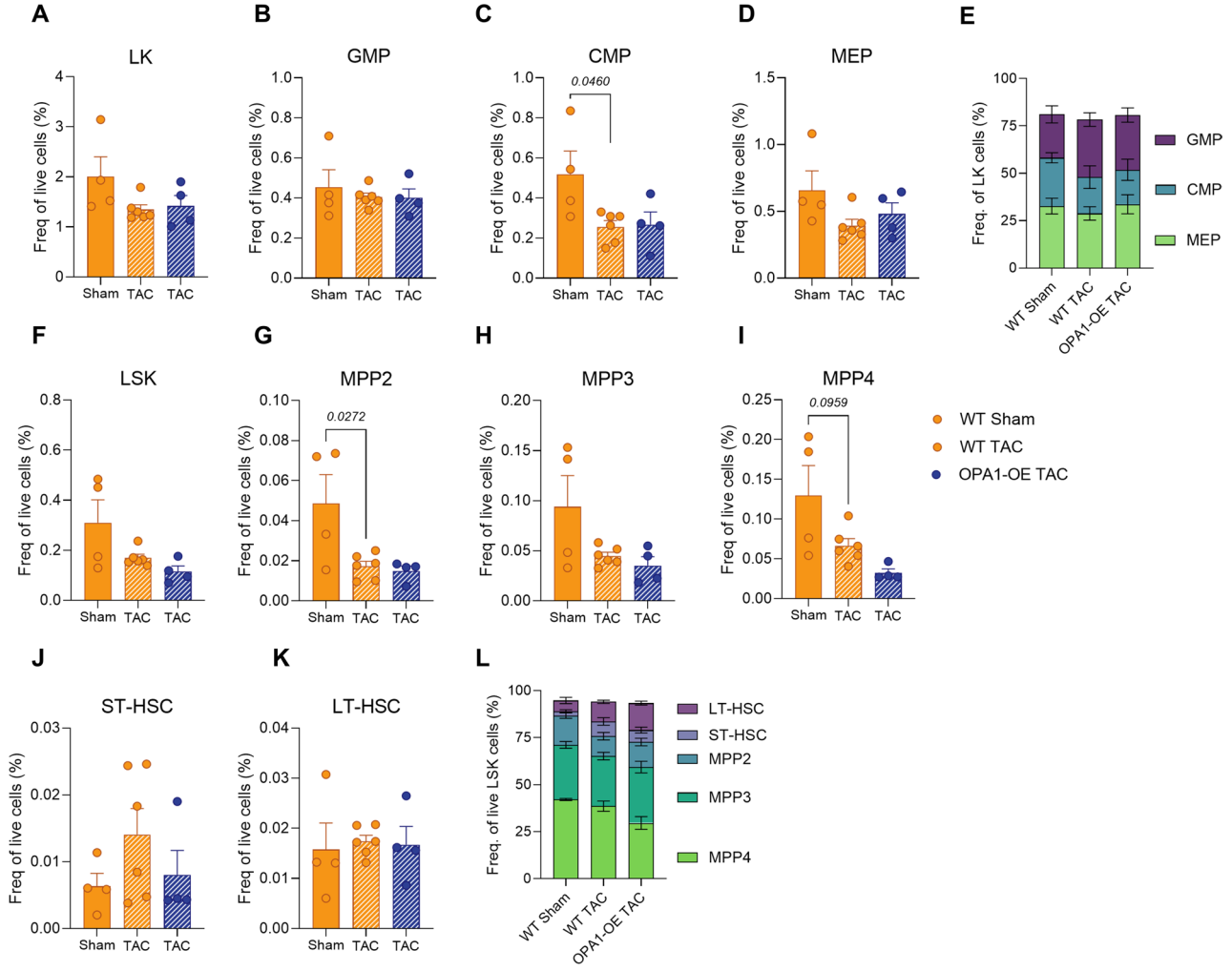

Fig. 8 Bone marrow progenitor populations are unchanged at 12 weeks post TAC. **A-E** Frequency of live LK (**A**), GMP (**B**), CMP (**C**), and MEP (**D**) cells, and ratio of all LK cells (**E**). **F-L** Frequency of live cells LSK (**F**), MPP2 (**G**), MPP3 (**H**), MPP4 (**I**), ST-HSC (**J**), and LT-HSC (**K**), and ratio of all LSK cells (**L**) in the bone marrow. $n = 4–6$ per group. All data are represented as mean ± SEM. *P* values calculated using a one-way ANOVA with Tukey's post-hoc analysis (**A**-**L**)

BW ratio. These results may explain how the OPA1-OE mice subjected to TAC resulted in increased HW/BW and HW/TL ratios, yet higher functional parameters compared to WT mice. OPA1 has also been implicated in protective cardiac remodeling in response to various treatment interventions in vivo such as empagliflozin [78, 79], irisin [80] and paeno1 [81]. These previous studies highlight OPA1 as a key mediator of protective cardiac phenotypes likely due to several mechanisms including its well characterized role in regulating cristae remodeling [82] and apoptotic signaling [10], mitochondrial fusion [83], mitochondrial supercomplex formation [45], oxidative metabolism [12], and calcium homeostasis [84].

Functional enrichment and protein-protein interaction network analyses of human LV samples demonstrated enriched cardiac contractile gene signatures associated with *OPA1* expression between top and bottom *OPA1* expression quintiles (Fig. 2). These data were supported by our 2D and 4D in vivo echocardiography findings showing that OPA1-OE mice have sustained cardiac function and myocardial kinetic motion compared to WT mice. Calcium signaling is critical for maintaining the function of contractile machinery in the heart [85]. In chronic heart failure, dysfunction of the ryanodine receptor 2 and dysfunction and downregulation of sarcoplasmic/endoplasmic reticulum Ca^{2+} ATPase 2a (SERCA2a) contribute to altered calcium signaling and disease progression [86]. Defects in calcium kinetics have been observed in *Opa1* heterozygous mice [19, 20]. Our data showing that OPA1-OE TAC mice had increased expression of the gene encoding SERCA2a (i.e., *Atp2a2*) compared to WT mice further support the importance of OPA1 in cardiac calcium signaling.

Another functional cluster identified from the protein-protein interaction network of the genes associated with *OPA1* expression was metabolic pathways such as

fatty acid and BCAA metabolism. Metabolic changes in heart failure involve alterations in substrate uptake and utilization. Our data further support the link between mitochondrial fusion and fatty acid oxidation previously identified in cardiac tissue [24]. Branched chain amino acid catabolism is another central metabolic pathway known to be decreased in heart failure and pressure-overload mouse models [87, 88]. We identified sustained transcript levels of certain BCAA enzymes in OPA1-OE TAC mice compared to WT TAC mice indicating a protective metabolic phenotype within our model. Heart failure is typically characterized by an "energy deficit" with decreases in electron transport chain activity or maximal oxidative capacity. Given this, we assessed various bioenergetic pathways, identifying no changes in oxidative capacity between sham and TAC mice in response to the sequential addition of fatty acid, and substrates for complex I and complex II of the electron transport chain. In addition, we did not identify changes in mitochondrial content. Previous in vivo work has shown that TAC induces changes in maximal oxidative capacity, mitochondrial enzymatic activities and the expression of mRNA and protein levels of various mitochondrial genes [89, 90]. Although these changes may be largely driven by decreases in overall mitochondrial content, our conflicting experimental results highlight important methodological considerations in assessing bioenergetic function. To assess maximal respiratory capacity, we used permeabilized myofibers and the sequential addition of saturating concentrations of various substrates as per standard bioenergetic protocols [91]. However, this does not fully represent in vivo steady state myocardial conditions, which may have been altered post-TAC. Future work could use protein and enzymatic activity approaches to confirm metabolic changes. The subpopulations of mitochondria within cardiac tissue including the subsarcolemmal and interfibrillar mitochondria are also differentially affected by pressure-overload [92] with interfibrillar mitochondria showing more significant decreases in respiratory capacity. In our experiments, we did not separate out these two populations so any functional differences may be masked by measuring the total myofiber response to the substrates.

Genes that were found to be significantly different in *OPA1* groups and negatively associated with *OPA1* levels in the GTEx LV samples included immune pathways such as cytokine and chemokine signaling. OPA1 has been shown to have critical roles in the innate [93, 94] and adaptive immune system [95]. In addition, loss of OPA1 in skeletal muscle leads to high levels of circulating inflammatory cytokines [61]. However, we did not observe any differences in bone marrow progenitor cell populations after TAC surgery between either genotype. This could be a matter of experimental timeline, as OPA1 may be important in the acute inflammatory response which peaks within 7 days of TAC surgery [69, 70]. In addition, OPA1 may play a protective role in inflammatory conditions of the heart such as viral myocarditis in which mitochondrial dynamics has been implicated in the immune responses [96, 97].

In our murine model of chronic heart failure, we opted to induce a less severe pressure overload, in which the descending aorta is constricted using a 26-gauge needle. This model allowed us to investigate chronic changes in cardiac function without inducing ubiquitous hypertrophy and fibrosis characteristic of high TAC models. Several methodologies have been developed to study heart failure pathology in mice since the original development of the TAC model [98]. Most TAC studies use transverse aortic banding with a 27-gauge needle, which induces rapid decreases in cardiac function and subsequent fibrotic remodeling evident within 2 weeks [99, 100]. Previous literature suggests that the placement of the aortic constriction affects the degree of pressure overload [63] and that the degree of constriction affects the severity of hypertrophic and fibrotic remodeling [100]. Direct comparisons of transverse aortic constriction with a 25-gauge, 26-gauge or 27-gauge needle has shown the differential hypertrophic and fibrotic remodeling in each model, with a 26-gauge constriction of the transverse aorta leading to moderate trends in hypertrophy and fibrosis [100]. Our use of a 26-gauge needle constricted around the descending aorta led to cardiac function remodeling confirmed by echocardiography and electrocardiogram analyses, and trends for increased hypertrophy and fibrosis. Although this mild phenotype may have masked genotypic changes that we would see in a more severe model of heart failure, it is interesting how OPA1 is protective even in a model that lacks an overt cardiac mitochondrial content or functional phenotype. Given how ejection fraction in OPA1-OE mice was significantly higher than WT mice even at 5 weeks, and this difference did not change through 12 weeks, it is possible that the higher OPA1 levels influenced the initial remodeling phase and exerted its protective effects at a timepoint not captured by our study. Future work will be needed to delineate the early impact of increased OPA1 levels at the onset of heart failure and development of hypertrophy and fibrosis in mouse models such as those employing modified pressure-overload induced cardiac stress with different degrees or sites of aortic constriction.

Conclusion

In conclusion, this study highlights the importance of OPA1 in mediating cardioprotective mechanisms. Our in silico approaches using publicly available human data identified associations between *OPA1* expression and cardiac tissue fibrosis as well as contractile and metabolic

pathways. Furthermore, our in vivo results support a role for OPA1 in mediating metabolic and contractile signaling. Overall, we provide evidence for the importance of OPA1 in cardiac function and elucidate gene signatures that underlie this protection.

Limitations and future directions

Our study has limitations that need to be addressed. First, we used a modified aortic banding around the descending aorta to induce pressure overload-induced cardiac stress. In our study, we saw preserved cardiac function in OPA1-OE mice compared to wildtype mice, but we cannot extrapolate these findings to a more severe pressure overload model such as the traditional TAC model which induces severe hypertrophy and fibrosis. To validate the cardiac remodeling process, we used alternative non-invasive measures such as ECG measures, which will be critical in the future use of this model along with improved descending aortic imaging. In addition, TAC surgeries can be subject to various technical complications that can affect the induction of pathological remodeling. Alternative methods to improve the consistency between surgeries, such as the double loop-clip approach [101] will be useful in future studies to minimize variability in the remodeling phenotype in our TAC model. The OPA1-OE mouse model exhibits a whole-body overexpression of OPA1, so we cannot exclude that non-cardiac OPA1 plays a role in the protective phenotype observed post-TAC. Future use of cardiac-specific models will be crucial to an improved understanding of tissue-specific and systemic contributions of OPA1 to cardioprotection. In addition, we did not assess OPA1 processing and isoforms, which has been elucidated in other cardiac studies [21–23]. Future work should employ advanced mouse models with cleavable and non-cleavable OPA1 isoforms [23] to further elucidate the role of OPA1 processing in chronic heart failure. All endpoint experiments in our study were conducted at 12 weeks post-TAC, which may have limited our findings as mitochondrial content has been shown to transiently increase post-TAC [67] and various immune signaling pathways are increased acutely after TAC surgery [69]. Instead, we focused on an extended timepoint at 12 weeks post-TAC to assess the role of OPA1 in a more chronic disease state. Investigating earlier time points in future studies may identify acute metabolic or immune mechanisms underlying the functional changes.

Abbreviations

IMM	Inner mitochondrial membrane
OMM	Outer mitochondrial membrane
DRP1	Dynamin-related protein 1
OPA1	Optic atrophy protein-1
TMM	Trimmed mean of M-values
LV	Left ventricle
GTEx	Genotype-Tissue Expression
PLS-DA	Partial least squares discriminant analysis
VIP	Variable importance projection
OPA1-OE	Optic atrophy protein-1 overexpressing
TAC	Transverse aortic constriction
LVEDD	Left ventricular end-diastolic diameter
LVESD	Left ventricular end-systolic diameter
WT	Wildtype
HW/BW	Heart weight/body weight
HW/TL	Heart weight/tibia length
EDV	End diastolic volume
ESV	End systolic volume
CSA	Cross-sectional area
BCAA	branched chain amino acid metabolism
CMP	Common myeloid progenitor
GMP	Granulocyte-monocyte progenitor
MEP	Megakaryocyte-erythroid progenitor
MPP	Multipotent progenitors
MPP3	Myeloid bias
MPP4	Lymphoid bias
MPP2	Erythroid bias
SERCA2a	Sarcoplasmic/endoplasmic reticulum Ca^{2+} ATPase 2a

Supplementary Information

The online version contains supplementary material available at https://doi.org/10.1186/s12872-025-05413-0.

Supplementary Material 1.

Supplementary Material 2.

Acknowledgements

We thank Dr. Luca Scorrano, Dr. Ruth Slack and Dr. Mireille Khacho for providing us with the OPA1-OE mice, Megan Fortier for technical assistance, Louise Pelletier Histology Core Facility (RRID: SCR_021737), Flow Cytometry and Virometry Core Facility (RRID: SCR_023306) for technical assistance, and the Animal Care and Veterinary Services at the University of Ottawa. We also acknowledge Conner C. Earl and the Cardiovascular Imaging Research Laboratory Group at Purdue University for their help and training with the 4D ultrasound graphical user interface and strain analysis code. Schematic figures were created using Biorender.com (publication license: KR28Q21BA8).

Clinical trial number

Not applicable.

Authors' contributions

CFM: Conceptualization, Methodology, Validation, Formal analysis, Investigation, Data curation, Writing – Original draft, Writing – Review & editing, Visualization. SMP: Methodology, Investigation, Writing – Review & editing. LSK: Methodology, Validation, Formal analysis, Investigation, Data curation, Writing – Original draft, Writing – Review & editing, Visualization. TKTS: Methodology, Formal analysis, Investigation, Writing – Review & editing, Visualization. SM: Investigation. MNK: Methodology, Formal analysis, Investigation. CYK: Methodology, Formal analysis, Investigation. MC: Investigation. MML: Formal analysis. EM: Investigation. ILS: Investigation. CJG: Software, Resources, Writing – Review & editing. MDF: Resources, Writing - Review & editing. MCC: Resources, Writing – Review & editing. EEM: Conceptualization, Resources, Writing- Original draft, Writing – review & editing, Supervision, Funding acquisition. MEH: Conceptualization, Resources, Writing- Original draft, Writing – review & editing, Supervision, Funding acquisition.

Funding

This work was funded by a Heart and Stroke Grant-in-Aid to M-E.H. and a New Investigator Award to E.E.M. and Canadian Institute of Health Research (E.E.M. Grant Number 186076, M-E.H. Grant Number 143278, M.D.F. Grant Number 148634). M-E.H. holds a Tier 1 Canada Research Chair in Mitochondrial Bioenergetics and Metabolic Health. MDF holds a Camille Villeneuve Chair in Cardiovascular Immunometabolism. CF-M and SMP were supported by Frederick Banting and Charles Best Canada Graduate Scholarships Doctoral Awards. L.K was supported by an Ontario Graduate Scholarship. T.K.T.S.

was supported by a Vanier Canada Scholarship. S.M. was supported by an OISB-NRC Graduate Student Scholarship. M.C. was supported by a Faculty of Medicine Summer Studentship Program Award.

Data availability

All bioinformatic data analyzed in this study are included in this published article and the supplementary information file. The other data generated from the current study are available from the corresponding author on reasonable request.

Declarations

Ethics approval and consent to participate

All experiments involving mice were conducted in accordance with the principles of the Canadian Council of Animal Care and were approved by the Animal Care Committee of the University of Ottawa (UOHI-AUP-2909 and AUP-4381).

Consent for publication

Not applicable.

Competing interests

Craig Goergen is a paid consultant of FUJIFILM VisualSonics Inc.

Received: 18 September 2025 / Accepted: 1 December 2025
Published online: 09 December 2025

References

1. Khan MS, Shahid I, Bennis A, Rakisheva A, Metra M, Butler J. Global epidemiology of heart failure. Nat Rev Cardiol. 2024;21(10):717–34.
2. Yan T, Zhu S, Yin X, Xie C, Xue J, Zhu M, et al. Burden, Trends, and inequalities of heart failure globally, 1990 to 2019: A secondary analysis based on the global burden of disease 2019 study. J Am Heart Assoc. 2023;12(6):e027852.
3. McDonald M, Virani S, Chan M, Ducharme A, Ezekowitz JA, Giannetti N, et al. CCS/CHFS Heart Failure Guidelines Update: Defining a New Pharmacologic Standard of Care for Heart Failure With Reduced Ejection Fraction. Can J Cardiol. 2021;37(4):531–46.
4. Sabbah HN. Targeting the mitochondria in heart failure. JACC Basic Transl Sci. 2020;5(1):88–106.
5. Brown DA, Perry JB, Allen ME, Sabbah HN, Stauffer BL, Shaikh SR, et al. Mitochondrial function as a therapeutic target in heart failure. Nat Rev Cardiol. 2017;14(4):238–50.
6. Hinton A, Claypool SM, Neikirk K, Senoo N, Wanjalla CN, Kirabo A, et al. Mitochondrial structure and function in human heart failure. Circ Res. 2024;135(2):372–96.
7. Chen Y, Liu Y, Dorn GW. Mitochondrial fusion is essential for organelle function and cardiac homeostasis. Circ Res. 2011;109(12):1327–31.
8. Wai T, Langer T. Mitochondrial dynamics and metabolic regulation. Trends Endocrinol Metab. 2016;27(2):105–17.
9. Mishra P, Carelli V, Manfredi G, Chan DC. Proteolytic cleavage of Opa1 stimulates mitochondrial inner membrane fusion and couples fusion to oxidative phosphorylation. Cell Metab. 2014;19(4):630–41.
10. Frezza C, Cipolat S, Martins De Brito O, Micaroni M, Beznoussenko GV, Rudka T, et al. OPA1 controls apoptotic cristae remodeling independently from mitochondrial fusion. Cell. 2006;126(1):177–89.
11. Del Dotto V, Fogazza M, Carelli V, Rugolo M, Zanna C. Eight human OPA1 isoforms, long and short: what are they for? Biochimica et Biophysica Acta (BBA). 2018;1859(4):263–9.
12. Del Dotto V, Mishra P, Vidoni S, Fogazza M, Maresca A, Caporali L, et al. OPA1 Isoforms in the Hierarchical Organization of Mitochondrial Functions. Cell Rep. 2017;20(12):2557–71.
13. Lee H, Smith SB, Yoon Y. The short variant of the mitochondrial dynamin OPA1 maintains mitochondrial energetics and cristae structure. J Biol Chem. 2017;292(17):7115–30.
14. Olichon A, Baricault L, Gas N, Guillou E, Valette A, Belenguer P, et al. Loss of OPA1 perturbs the mitochondrial inner membrane structure and integrity, leading to cytochrome c release and apoptosis. J Biol Chem. 2003;278(10):7743–6.
15. Varanita T, Soriano ME, Romanello V, Zaglia T, Quintana-Cabrera R, Semenzato M, et al. The OPA1-dependent mitochondrial cristae remodeling pathway controls atrophic, apoptotic, and ischemic tissue damage. Cell Metab. 2015;21(6):834–44.
16. Lee H, Smith SB, Sheu SS, Yoon Y. The short variant of optic atrophy 1 (OPA1) improves cell survival under oxidative stress. J Biol Chem. 2020;295(19):6543–60.
17. Chen L, Gong Q, Stice JP, Knowlton AA. Mitochondrial OPA1, apoptosis, and heart failure. Cardiovasc Res. 2009;84(1):91–9.
18. Sabbah HN, Gupta RC, Singh-Gupta V, Zhang K, Lanfear DE. Abnormalities of mitochondrial dynamics in the failing heart: normalization following long-term therapy with Elamipretide. Cardiovasc Drugs Ther. 2018;32(4):319–28.
19. Piquereau J, Caffin F, Novotova M, Prola A, Garnier A, Mateo P, et al. Down-regulation of OPA1 alters mouse mitochondrial morphology, PTP function, and cardiac adaptation to pressure overload. Cardiovasc Res. 2012;94(3):408–17.
20. Chen L, Liu T, Tran A, Lu X, Tomilov AA, Davies V, et al. OPA1 mutation and late-onset cardiomyopathy: mitochondrial dysfunction and mtDNA instability. J Am Heart Assoc. 2012;1(5):e003012.
21. Wai T, García-Prieto J, Baker MJ, Merkwirth C, Benit P, Rustin P, et al. Imbalanced OPA1 processing and mitochondrial fragmentation cause heart failure in mice. Science. 2015;350(6265):aad0116.
22. Acin-Perez R, Lechuga-Vieco AV, Del Mar Muñoz M, Nieto-Arellano R, Torroja C, Sánchez-Cabo F, et al. Ablation of the stress protease OMA1 protects against heart failure in mice. Sci Transl Med. 2018;10(434):eaan4935.
23. Ahola S, Pazurek LA, Mayer F, Lampe P, Hermans S, Becker L, et al. Opa1 processing is dispensable in mouse development but is protective in mitochondrial cardiomyopathy. Sci Adv. 2024;10(31):eadp0443.
24. Guo Y, Wang Z, Qin X, Xu J, Hou Z, Yang H, et al. Enhancing fatty acid utilization ameliorates mitochondrial fragmentation and cardiac dysfunction via rebalancing optic atrophy 1 processing in the failing heart. Cardiovasc Res. 2018;114(7):979–91.
25. Semenzato M, Kohr MJ, Quirin C, Menabò R, Alanova P, Alan L, et al. Oxidization of optic atrophy 1 cysteines occurs during heart ischemia-reperfusion and amplifies cell death by oxidative stress. Redox Biol. 2023;63:102755.
26. Hunter JD. Matplotlib: a 2D graphics environment. Comput Sci Eng. 2007;9(3):90–5.
27. Waskom M. Seaborn: statistical data visualization. J Open Source Softw. 2021;6(60):3021.
28. Virtanen P, Gommers R, Oliphant TE, Haberland M, Reddy T, Cournapeau D, et al. SciPy 1.0: fundamental algorithms for scientific computing in python. Nat Methods. 2020;17(3):261–72.
29. Robinson MD, Oshlack A. A scaling normalization method for differential expression analysis of RNA-seq data. Genome Biol. 2010;11(3):R25.
30. Hardy JA, Wester P, Winblad B, Gezelius C, Bring G, Eriksson A. The patients dying after long terminal phase have acidotic brains; implications for biochemical measurements on autopsy tissue. J Neural Transm. 1985;61(3–4):253–64.
31. Biospecimen Research Database .Bethesda (MD). National Cancer Institute, Biorepositories and Biospecimen Research Branch. Available from http://biospecimens.cancer.gov/brd [cited 2024 Aug 15].
32. Seabold S, Perktold J. statsmodels: Econometric and statistical modeling with python. Proceedings of the 9th Python in Science Conference. 2010. In.
33. Wold S, Sjöström M, Eriksson L. PLS-regression: a basic tool of chemometrics. Chemom Intell Lab Syst. 2001;58(2):109–30.
34. Kira K, Rendell LA. A Practical Approach to Feature Selection. In: Machine Learning Proceedings 1992. Elsevier; 1992 . pp. 249–56. Available from: https://linkinghub.elsevier.com/retrieve/pii/B9781558602472500371 [cited 2024 Aug 15].
35. Moore JH, White BC. Tuning ReliefF for Genome-Wide Genetic Analysis. In: Marchiori E, Moore JH, Rajapakse JC, editors. Evolutionary Computation,Machine Learning and Data Mining in Bioinformatics. Berlin, Heidelberg: Springer Berlin Heidelberg; 2007. pp. 166–75. (Lecture Notes in Computer Science; vol. 4447). Available from: http://link.springer.com/ https://doi.org/10.1007/978-3-540-71783-6_16 [cited 2024 Aug 15].
36. Pedregosa F, Varoquaux G, Gramfort A, Michel V, Thirion B, Grisel O, et al. Scikit-learn: machine learning in python. J Mach Learn Res. 2011;12(85):2825–30.
37. Urbanowicz RJ, Olson RS, Schmitt P, Meeker M, Moore JH. Benchmarking relief-based feature selection methods for bioinformatics data mining. J Biomed Inform. 2018;85:168–88.
38. Kononenko I. Estimating attributes: Analysis and extensions of RELIEF. In: Bergadano F, Raedt L,Machine Learning: ECML-94., Berlin H. 1994. pp. 171–82.

(Carbonell JG, Siekmann J, Goos G, Hartmanis J, editors. Lecture Notes in Computer Science; vol. 784). Available from: http://link.springer.com/ https://doi.org/10.1007/3-540-57868-4_57 [cited 2024 Aug 15].
39. Andersen CM, Bro R. Variable selection in regression—a tutorial. J Chemom. 2010;24(11–12):728–37.
40. Urbanowicz RJ, Meeker M, La Cava W, Olson RS, Moore JH. Relief-based feature selection: introduction and review. J Biomed Inform. 2018;85:189–203.
41. Ge SX, Jung D, Yao R. ShinyGO: a graphical gene-set enrichment tool for animals and plants. Valencia A, editor. Bioinformatics. 2020;36(8):2628–9.
42. The Gene Ontology Consortium. The gene ontology resource: 20 years and still going strong. Nucleic Acids Res. 2019;47(D1):D330–8.
43. Szklarczyk D, Gable AL, Nastou KC, Lyon D, Kirsch R, Pyysalo S, et al. The STRING database in 2021: customizable protein–protein networks, and functional characterization of user-uploaded gene/measurement sets. Nucleic Acids Res. 2021;49(D1):D605–12.
44. Szklarczyk D, Kirsch R, Koutrouli M, Nastou K, Mehryary F, Hachilif R, et al. The STRING database in 2023: protein–protein association networks and functional enrichment analyses for any sequenced genome of interest. Nucleic Acids Res. 2023;51(D1):D638–46.
45. Cogliati S, Frezza C, Soriano ME, Varanita T, Quintana-Cabrera R, Corrado M, et al. Mitochondrial Cristae shape determines respiratory chain supercomplexes assembly and respiratory efficiency. Cell. 2013;155(1):160–71.
46. Damen FW, Salvas JP, Pereyra AS, Ellis JM, Goergen CJ. Improving characterization of hypertrophy-induced murine cardiac dysfunction using four-dimensional ultrasound-derived strain mapping. Am J Physiol-Heart Circ Physiol. 2021;321(1):H197-207.
47. Dann MM, Clark SQ, Trzaskalski NA, Earl CC, Schepers LE, Pulente SM, et al. Quantification of murine myocardial infarct size using 2-D and 4-D high-frequency ultrasound. Am J Physiol Heart Circ Physiol. 2022;322(3):H359–72.
48. Damen FW, Gramling DP, Ahlf Wheatcraft D, Wilpan RY, Costa MW, Goergen CJ. Application of 4-D ultrasound-derived regional strain and proteomics analysis in *Nkx2-5* -deficient male mice. Am J Physiol-Heart Circ Physiol. 2023;325(2):H293-310.
49. Oestereicher MA, Wotton JM, Ayabe S, Bou About G, Cheng TK, Choi JH, et al. Comprehensive ECG reference intervals in C57BL/6N substrains provide a generalizable guide for cardiac electrophysiology studies in mice. Mamm Genome Off J Int Mamm Genome Soc. 2023;34(2):180–99.
50. Stringer C, Wang T, Michaelos M, Pachitariu M. Cellpose: a generalist algorithm for cellular segmentation. Nat Methods. 2021;18(1):100–6.
51. Spinazzi M, Casarin A, Pertegato V, Salviati L, Angelini C. Assessment of mitochondrial respiratory chain enzymatic activities on tissues and cultured cells. Nat Protoc. 2012;7(6):1235–46.
52. Guo W, Jiang L, Bhasin S, Khan SM, Swerdlow RH. DNA extraction procedures meaningfully influence qPCR-based MtDNA copy number determination. Mitochondrion. 2009;9(4):261–5.
53. Livak KJ, Schmittgen TD. Analysis of relative gene expression data using real-time quantitative PCR and the 2 – ΔΔCT method. Methods. 2001;25(4):402–8.
54. Mann HB, Whitney DR. On a test of whether one of two random variables is stochastically larger than the other. Ann Math Stat. 1947;18(1):50–60.
55. Student. The probable error of a mean. Biometrika. 1908;6(1):1–25.
56. Pearson KX. On the criterion that a given system of deviations from the probable in the case of a correlated system of variables is such that it can be reasonably supposed to have arisen from random sampling. Lond Edinb Dublin Philos Mag J Sci. 1900;50(302):157–75.
57. Lonsdale J, Thomas J, Salvatore M, Phillips R, Lo E, Shad S, et al. The Genotype-Tissue Expression (GTEx) project. Nat Genet. 2013;45(6):580–5.
58. GTEx Consortium. Genetic effects on gene expression across human tissues. Nature. 2017;550(7675):204–13.
59. Ali MA, Gioscia-Ryan R, Yang D, Sutton NR, Tyrrell DJ. Cardiovascular aging: spotlight on mitochondria. Am J Physiol Heart Circ Physiol. 2024;326(2):H317-33.
60. Lesnefsky EJ, Chen Q, Hoppel CL. Mitochondrial metabolism in aging heart. Circ Res. 2016;118(10):1593–611.
61. Tezze C, Romanello V, Desbats MA, Fadini GP, Albiero M, Favaro G, et al. Age-Associated loss of OPA1 in muscle impacts muscle Mass, metabolic Homeostasis, systemic Inflammation, and epithelial senescence. Cell Metab. 2017;25(6):1374-e13896.
62. Carithers LJ, Ardlie K, Barcus M, Branton PA, Britton A, Buia SA, et al. A novel approach to high-quality postmortem tissue procurement: the GTEx project. Biopreserv Biobank. 2015;13(5):311–9.
63. Tarnavski O, McMullen JR, Schinke M, Nie Q, Kong S, Izumo S. Mouse cardiac surgery: comprehensive techniques for the generation of mouse models of human diseases and their application for genomic studies. Physiol Genomics. 2004;16(3):349–60.
64. Lopaschuk GD, Karwi QG, Tian R, Wende AR, Abel ED. Cardiac energy metabolism in heart failure. Circ Res. 2021;128(10):1487–513.
65. Ribeiro Junior RF, Dabkowski ER, Shekar KC, O´Connell KA, Hecker PA, Murphy MP. MitoQ improves mitochondrial dysfunction in heart failure induced by pressure overload. Free Radic Biol Med. 2018;117:18–29.
66. Dai DF, Hsieh EJ, Liu Y, Chen T, Beyer RP, Chin MT, et al. Mitochondrial proteome remodelling in pressure overload-induced heart failure: the role of mitochondrial oxidative stress. Cardiovasc Res. 2012;93(1):79–88.
67. Shirakabe A, Zhai P, Ikeda Y, Saito T, Maejima Y, Hsu CP, et al. Drp1-dependent mitochondrial autophagy plays a protective role against pressure overload–induced mitochondrial dysfunction and heart failure. Circulation. 2016;133(13):1249–63.
68. Marvasti TB, Alibhai FJ, Yang GJ, Li S, Wu J, Yau T et al. Heart Failure Impairs Bone Marrow Hematopoietic Stem Cell Function and Responses to Injury. J Am Heart Assoc. 2023 ;12(11):e027727.
69. Xia Y, Lee K, Li N, Corbett D, Mendoza L, Frangogiannis NG. Characterization of the inflammatory and fibrotic response in a mouse model of cardiac pressure overload. Histochem Cell Biol. 2009;131(4):471–81.
70. Martini E, Kunderfranco P, Peano C, Carullo P, Cremonesi M, Schorn T, et al. Single-cell sequencing of mouse heart immune infiltrate in pressure overload–driven heart failure reveals extent of immune activation. Circulation. 2019;140(25):2089–107.
71. Kleiner JL, Köpke O, Faron A, Zhang Y, Cornelssen J, Coburn M et al. Characterization of Transverse Aortic Constriction in Mice Based on the Specific Recruitment of Leukocytes to the Hypertrophic Myocardium and the Aorta Ascendens. Kennedy S, editor. Mediators Inflamm. 2021;2021:1376859.
72. Almind GJ, Ek J, Rosenberg T, Eiberg H, Larsen M, LuCamp L, et al. Dominant optic atrophy in Denmark – report of 15 novel mutations in OPA1, using a strategy with a detection rate of 90%. BMC Med Genet. 2012;13(1):65.
73. Ferré M, Bonneau D, Milea D, Chevrollier A, Verny C, Dollfus H, et al. Molecular screening of 980 cases of suspected hereditary optic neuropathy with a report on 77 novel *OPA1* mutations. Hum Mutat. 2009;30(7):E692-705.
74. Liguori M, Russa A, Manna I, Andreoli V, Caracciolo M, Spadafora P, et al. A phenotypic variation of dominant optic atrophy and deafness (ADOAD) due to a novel OPA1 mutation. J Neurol. 2008;255(1):127–9.
75. Liskova P, Ulmanova O, Tesina P, Melsova H, Diblik P, Hansikova H, et al. Novel *OPA1* missense mutation in a family with optic atrophy and severe widespread neurological disorder. Acta Ophthalmol (Copenh). 2013;91(3):e225-231.
76. Hudson G, Amati-Bonneau P, Blakely EL, Stewart JD, He L, Schaefer AM, et al. Mutation of *OPA1* causes dominant optic atrophy with external ophthalmoplegia, ataxia, deafness and multiple mitochondrial DNA deletions: a novel disorder of MtDNA maintenance. Brain. 2008;131(2):329–37.
77. Le Page S, Niro M, Fauconnier J, Cellier L, Tamareille S, Gharib A et al. Increase in Cardiac Ischemia-Reperfusion Injuries in Opa1+/- Mouse Model. Bertrand L, editor. PLOS ONE. 2016;11(10):e0164066.
78. Cai W, Chong K, Huang Y, Huang C, Yin L. Empagliflozin improves mitochondrial dysfunction in diabetic cardiomyopathy by modulating ketone body metabolism and oxidative stress. Redox Biol. 2024;69:103010.
79. Lyu Y, Huo J, Jiang W, Yang W, Wang S, Zhang S, et al. Empagliflozin ameliorates cardiac dysfunction in heart failure mice via regulating mitochondrial dynamics. Eur J Pharmacol. 2023;942:175531.
80. Xin T, Lu C. Irisin activates Opa1-induced mitophagy to protect cardiomyocytes against apoptosis following myocardial infarction. Aging. 2020;12(5):4474–88.
81. Liu C, Han Y, Gu X, Li M, Du Y, Feng N, et al. Paeonol promotes Opa1-mediated mitochondrial fusion via activating the CK2α-Stat3 pathway in diabetic cardiomyopathy. Redox Biol. 2021;46:102098.
82. Patten DA, Wong J, Khacho M, Soubannier V, Mailloux RJ, Pilon-Larose K, et al. OPA1-dependent Cristae modulation is essential for cellular adaptation to metabolic demand. EMBO J. 2014;33(22):2676–91.
83. Cipolat S, Martins de Brito O, Dal Zilio B, Scorrano L. *OPA1* requires Mitofusin 1 to promote mitochondrial fusion. Proc Natl Acad Sci U S A. 2004;101(45):15927–32.
84. Kushnareva YE, Gerencser AA, Bossy B, Ju WK, White AD, Waggoner J, et al. Loss of OPA1 disturbs cellular calcium homeostasis and sensitizes for excitotoxicity. Cell Death Differ. 2013;20(2):353–65.
85. Fearnley CJ, Roderick HL, Bootman MD. Calcium signaling in cardiac myocytes. Cold Spring Harb Perspect Biol. 2011;3(11):a004242–004242.

86. Marks AR. Calcium cycling proteins and heart failure: mechanisms and therapeutics. J Clin Invest. 2013;123(1):46–52.
87. Sun H, Olson KC, Gao C, Prosdocimo DA, Zhou M, Wang Z, et al. Catabolic defect of branched-chain amino acids promotes heart failure. Circulation. 2016;133(21):2038–49.
88. Uddin GM, Zhang L, Shah S, Fukushima A, Wagg CS, Gopal K, et al. Impaired branched chain amino acid oxidation contributes to cardiac insulin resistance in heart failure. Cardiovasc Diabetol. 2019;18(1):86.
89. Garnier A, Fortin D, Deloménie C, Momken I, Veksler V, Ventura-Clapier R. Depressed mitochondrial transcription factors and oxidative capacity in rat failing cardiac and skeletal muscles. J Physiol. 2003;551(2):491–501.
90. Abdurrachim D, Nabben M, Hoerr V, Kuhlmann MT, Bovenkamp P, Ciapaite J, et al. Diabetic db/db mice do not develop heart failure upon pressure overload: a longitudinal in vivo PET, MRI, and MRS study on cardiac metabolic, structural, and functional adaptations. Cardiovasc Res. 2017;113(10):1148–60.
91. Schmidt CA, Fisher-Wellman KH, Neufer PD. From OCR and ECAR to energy: perspectives on the design and interpretation of bioenergetics studies. J Biol Chem. 2021;297(4):101140.
92. Schwarzer M, Schrepper A, Amorim PA, Osterholt M, Doenst T. Pressure overload differentially affects respiratory capacity in interfibrillar and subsarcolemmal mitochondria. Am J Physiol-Heart Circ Physiol. 2013;304(4):H529–37.
93. Sánchez-Rodríguez R, Tezze C, Agnellini AHR, Angioni R, Venegas FC, Cioccarelli C, et al. OPA1 drives macrophage metabolism and functional commitment via p65 signaling. Cell Death Differ. 2023;30(3):742–52.
94. Amini P, Stojkov D, Felser A, Jackson CB, Courage C, Schaller A, et al. Neutrophil extracellular trap formation requires OPA1-dependent glycolytic ATP production. Nat Commun. 2018;9(1):2958.
95. Corrado M, Samardžić D, Giacomello M, Rana N, Pearce EL, Scorrano L. Deletion of the mitochondria-shaping protein Opa1 during early thymocyte maturation impacts mature memory T cell metabolism. Cell Death Differ. 2021;28(7):2194–206.
96. Jin U, Park SJ, Lee BG, Kim JB, Kim SJ, Joe EH, et al. Critical roles of parkin and PINK1 in coxsackievirus B3-induced viral myocarditis. Microbes Infect. 2023;25(8):105211.
97. Mohamud Y, Li B, Bahreyni A, Luo H. Mitochondria dysfunction at the heart of viral myocarditis: mechanistic insights and therapeutic implications. Viruses. 2023;15(2):351.
98. Rockman HA, Ross RS, Harris AN, Knowlton KU, Steinhelper ME, Field LJ, et al. Segregation of atrial-specific and inducible expression of an atrial natriuretic factor transgene in an in vivo murine model of cardiac hypertrophy. Proc Natl Acad Sci U S A. 1991;15(18):8277–81.
99. Huang M, Yu L, Wang X, Wang M, Li W, Tang J, et al. Evaluation of the transverse aortic constriction model in ICR and C57BL/6J mice. Front Physiol. 2022;13:1026884.
100. Richards DA, Aronovitz MJ, Calamaras TD, Tam K, Martin GL, Liu P, et al. Distinct phenotypes induced by three degrees of transverse aortic constriction in mice. Sci Rep. 2019;9(1):5844.
101. Merino D, Gil A, Gómez J, Ruiz L, Llano M, García R, et al. Experimental modelling of cardiac pressure overload hypertrophy: modified technique for precise, reproducible, safe and easy aortic arch banding-debanding in mice. Sci Rep. 2018;8:3167.

Publisher's Note